AD-A256 682

ON PAGE

1. AGENCY USE ONLY (Leave blank)	2. REPORT DATE 17 August 1992	3. REPORT TYPE AND DATES COVERED Reprint

4. TITLE AND SUBTITLE Phenomenology of a Water Venting in Low Earth Orbit	5. FUNDING NUMBERS
6. AUTHOR(S) I.L. Kofsky*, D.L.A. Rall*, M.A.Maris*, N.H. Tran*, E. Murad, C.P. Pike, D.J. Knecht, R.A. Viereck, A.T.Stair, Jr.**, A. Setayesh#	PE 62101F PR 7601 TA 30 WU 06

7. PERFORMING ORGANIZATION NAME(S) AND ADDRESS(ES) Phillips Lab/WSSI Hanscom AFB Massachusetts 01731-5000	8. PERFORMING ORGANIZATION REPORT NUMBER PL-TR-92-2212

DTIC
ELECTE
AUG 2 5 1992
S
C
D

9. SPONSORING/MONITORING AGENCY NAME(S) AND ADDRESS(ES)	10. SPONSORING/MONITORING AGENCY REPORT NUMBER

12a. DISTRIBUTION/AVAILABILITY STATEMENT Approved for public release; Distribution unlimited	12b. DISTRIBUTION CODE

13. ABSTRACT (Maximum 200 words)

Abstract—Venting of excess water from spacecraft, besides leading to physical and optical contamination, has application to studies of the transport of outgas, the interaction of the vehicle with the ionospheric plasma, the energy balance of cometary material, and the uses of liquid streams in space operations. Analysis of intensified video images of a twilight venting of fuel-cell product water from Shuttle Orbiter shows that the initially coherent stream forms within about 0.1 s into a ~10°-quasiconical cloud of irregular, polydisperse ice/water droplets (the product of cavitational rupturing) and submicron ice spherules (from partial recondensation of overexpanded vacuum-evaporated water gas). The retrograde velocities of both particle components are experimentally indistinguishable from that calculated for the dumped liquid. The visible radiance distribution of the ~2½ km of wake trail detectable in projections to a precisely-tracked groundbased telescope becomes consistent with predictions from the energy balance of the submicron particles when a sublimation rate-enhancing correction to their emissivities (and thus temperature), arising from the progressive roughening of their surfaces, is applied. A similar calculation of the thermal radiation, scattering and absorption of earthshine and sunlight, and sublimation of the larger (~mm-radius) particles prominent in the onboard photographs shows that their lifetimes are several orbital periods. The relative discrete and spatially-continuous irradiances in images from the two camera locations impose a rough joint constraint on the fraction of water vapor that recondenses and the mean geometric scattering cross-section of the stream-fragmentation droplets.

14. SUBJECT TERMS Liquid water, Venting, Space, Phenomenology	15. NUMBER OF PAGES 23
	16. PRICE CODE

17. SECURITY CLASSIFICATION OF REPORT Unclassified	18. SECURITY CLASSIFICATION OF THIS PAGE Unclassified	19. SECURITY CLASSIFICATION OF ABSTRACT Unclassified	20. LIMITATION OF ABSTRACT SAR

Standard Form 298 (Rev. 2-89)

PL-TR-92-2212

PHENOMENOLOGY OF A WATER VENTING IN LOW EARTH ORBIT

I. L. KOFSKY, D. L. A. RALL, M. A. MARIS and N. H. TRAN

PhotoMetrics, Inc., 4 Arrow Drive, Woburn, MA 01801 U.S.A.

E. MURAD, C. P. PIKE. D. J. KNECHT and R. A. VIERECK

Geophysics Directorate, Phillips Laboratory (USAFSC), Hanscom AFB, MA 01731, U.S.A.

A. T. STAIR JR

A. T. Stair Associates, 139 Great Road, Bedford, MA 01730, U.S.A.

and

A. SETAYESH

Radex, Inc., 3 Preston Court, Bedford, MA 01730, U.S.A.

Abstract—Venting of excess water from spacecraft, besides leading to physical and optical contamination, has application to studies of the transport of outgas, the interaction of the vehicle with the ionospheric plasma, the energy balance of cometary material, and the uses of liquid streams in space operations. Analysis of intensified video images of a twilight venting of fuel-cell product water from Shuttle Orbiter shows that the initially coherent stream forms within about 0.1 s into a $\sim 10^5$-quasiconical cloud of irregular, polydisperse ice/water droplets (the product of cavitational rupturing) and submicron ice spherules (from partial recondensation of overexpanded vacuum-evaporated water gas). The retrograde velocities of both particle components are experimentally indistinguishable from that calculated for the dumped liquid. The visible radiance distribution of the $\sim 2\frac{1}{2}$ km of wake trail detectable in projections to a precisely-tracked groundbased telescope becomes consistent with predictions from the energy balance of the submicron particles when a sublimation rate-enhancing correction to their emissivities (and thus temperature), arising from the progressive roughening of their surfaces, is applied. A similar calculation of the thermal radiation, scattering and absorption of earthshine and sunlight, and sublimation of the larger ($\sim$ mm-radius) particles prominent in the onboard photographs shows that their lifetimes are several orbital periods. The relative discrete and spatially-continuous irradiances in images from the two camera locations impose a rough joint constraint on the fraction of water vapor that recondenses and the mean geometric scattering cross-section of the stream-fragmentation droplets.

1. INTRODUCTION

We have reduced and interpreted the patterns of scattering of visible sunlight by the ice particles that formed [1,2] from fuel cell-product water [3] vented into the wake of Shuttle Orbiter *Discovery* (STS-29, Orbit 49) just before dawn on 16 March 1989. The data set consists of intensified-video photographs taken from both onboard and a high-altitude optical station near the trajectory nadir. Table 1 describes the three electronic cameras, typical views of the particle clouds from which are reproduced in Figs 1–3.

The information about the phenomenology of ventings of excess water derived from these images allows the radiance distributions of these clouds at other wavelengths to be inferred, for assessing the effect of releases of high vapor pressure liquids on the optical signatures of satellites and suborbital bodies. The data on droplet sizes and fractionation, spatial and velocity distributions, and sublimation rates in the low earth-orbital environment also have application to several issues in space operations and physics, including foregrounds [4] in Shuttle-borne astronomy and remote sensing; lifetimes of orbiting debris, and the energy balance of comets and meteors; interaction of spacecraft [3] and their outgassed water vapor [5] with the ionosphere; F-region plasma depletion and its related aerochemical and dynamical effects [6]; and contamination of the outer surfaces of orbiting vehicles by recontact of ejected material [2]. Applications of controlled liquid streams in astronautics have been identified in a recent review [7] of their behavior in vacuum, and include material transport between spacecraft, liquid thrusters and brakes ("aeroassist"), fluid disposal, liquid-droplet radiators, and planetary gas scavenging.

2. TECHNICAL BACKGROUND

This theoretical modeling [7] is supported by recent laboratory simulations [8-11] in which pure and mildly contaminated water was released into large vacuum chambers with about the same initial flow conditions as in space shuttle's now-routine vent-ings. The outermost layers of the liquid quasicylin-der become cooled by the very rapid evaporation from its surface, while the low heat transport rate of water maintains the volume near its axis at close to the injection temperature. Since this inner water mass is then superheated, bubbles of "steam" and dissolved gases expand rapidly within the coherent stream; as they break through its surface, surface tension-driven instabilities tear the stream apart. While existing theory does not explicitly predict the velocities imparted to the resulting dis-crete liquid droplets, the halfwidth of the spatial distributions of these particles observed in labora-tory experiments [9-11], ~1·5 radian, provides a measure of their mean transverse speed relative to the longitudinal flow.

The droplets produced in this "flash evaporation" were found [8,10,11] to have typical dimensions comparable with the initial diameter of the liquid stream, as might be expected. Photographs from one experiment [8] showed them to take on dish or bowl shapes, which was interpreted as due to cracking of their ice surfaces by the higher pressure of the unfrozen, less dense inner water; the particles imaged may actually be fragments of larger droplets that fractured as successive shells solidified as a result of the heat loss by surface sublimation. The distri-bution of maximum droplet dimensions was broad (halfwidth about twice the injection-nozzle diameter), with most of the volume appearing in the largest individual particles. (We observed a qualitatively similar wide size spread in the onboard video images, as discussed in Section 4.2.)

These irregular droplets solidify completely (the larger ones would experience further explosive boil-ing, or breakup by cracking) in a time that we estimate in Appendix B to be 10 s. Cavitational rupturing takes place within < ~1 m from the venting nozzle when the initial diameter is > ~1/2 mm [9]; thinner, cold, pure water streams can propagate stably [7], while warm contaminated streams have been observed to break apart within a few nozzle diameters [9]. Since the heat of vaporization of water is large compared with the sum of its heat of fusion and the heat liberated when the liquid and then solid cool, most of the vented water appears as these large particles: simple thermodynamic arguments [6] show that the fraction of 0 C ice is 0.8 when water is injected at temperatures near 60 C, and the further sub-limative cooling to the ~180 K daytime equi-librium temperature calculated in Appendix B reduces this fraction to about 0.75.

The mean free paths of those water molecules that have evaporated from the short-lived coherent stream are initially much less than its diameter [9] (and a fortiori also small compared with the transverse extent of the cloud of droplets just after the stream bursts), so that the initial expansion of this vapor is collisional. This gas then cools as it expands further radially, and when it becomes supersaturated—that is, falls below the gas-solid phase boundary—some of it recondenses into ice particles. Radii near 0.1 μm (and a relatively monodisperse size distribution, rem-iniscent of that found in fog formed by adiabatic expansion of water vapor) were inferred from the polarization ratios of Mie scattering of laser light in a tank experiment [10,11] in which the water was injected in 65 μs-duration pulses. The fraction of the water molecules condensed into these particles was estimated [11] as between 0.2 and 2%, which represents 1·100–1·10 of the flash-vaporized water mass.

This (and previous referenced [7,9]) earlier work, much of which was done in connection with the design of systems for dumping excess water from orbiting spacecraft, indicates that the radiation pat-terns in Figs 1-3 result from reflection/refraction of sunlight from ~mm and submicron particles. The contribution to the signal from the much less efficiently (Rayleigh) scattering evaporated/sublimed water molecules would be expected to be negligible, and indeed the vapor phase has not been directly optically detectable in either laboratory simulations or the present space experiment.

3. EXPERIMENT

Relatively pure and gas-free "supply" (as opposed to human waste [3]) water was forced out under pressure into a retrograde orbit through a smooth 60 full-angle conical nozzle with a 1.4-mm (0.056-in.) diameter opening, at an essentially constant rate of 19.4 g/s. The venting orifice was electrically heated to prevent its blockage by icing (as had occurred in previous spacecraft missions), which gave the water an initial temperature that we estimate from the workspace temperature [9] and the time that the stream was in contact with the 60-70 C outlet tube to be 30 C. The vehicle aspect data and a diagram of the water-dumping system provided by NASA showed that the initial flow direction was antiparallel to Discovery's trajectory within less than 3 (indeed, perhaps < 1).

The spacecraft was oriented with long axis pitched 111 down from the local horizontal—the normal to its open bay directed toward the atmosphere's limb—and starboard wing toward the flight direction. Its venting nozzle is located [3] on its port side about 3 m below (on the vehicle: above in this flight orien-tation) and aft of crew cabin window W1, at station 620.0, −105.0, 342.6 [in.] in space shuttle system
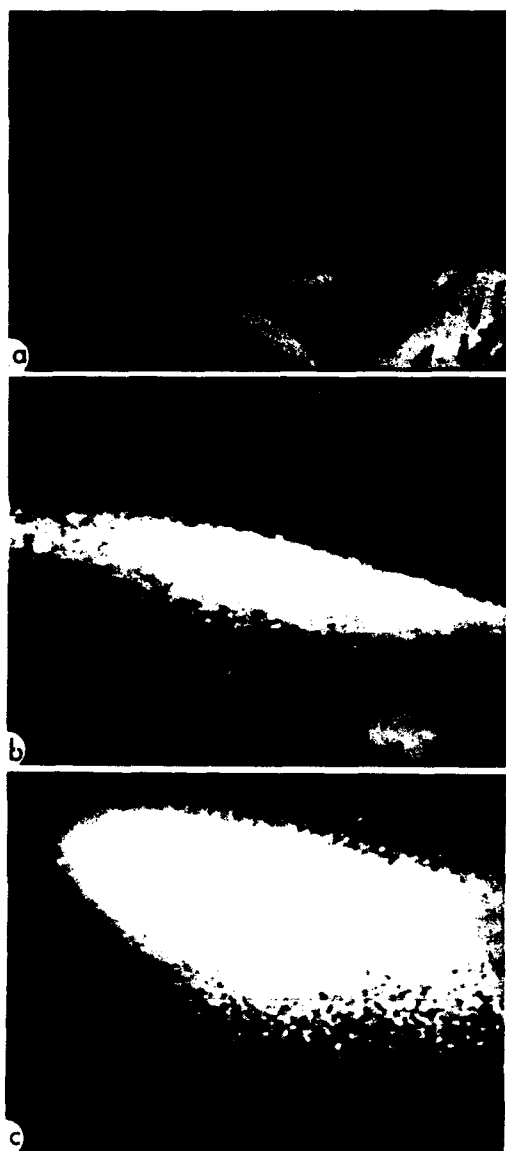
Fig. 1. Views of the backlit water trail from the aft onboard camera at increasing pointing azimuths. The determination of particle velocity in Section 4.2.2 was made from successive frames at the zoom setting and radiance response of (b). (b) The rainbow-angle region near the bright center of the frame. (c) Includes the vanishing point of the trail, at upper left. Some of the individual large droplets scatter sufficiently strongly to produce undershoots in the video electronics; other dark areas in the images are most likely regions of low particle density.

views from *Discovery's* cabin. Each of these cameras could see the trail to within about 5 m from its venting orifice.

Geophysics Directorate staff planned the water dump to be directly illuminated by the sun while the lower atmosphere above the groundbased telescope-camera (and below the onboard cameras) remained in the hard earth's shadow. The spacecraft was in a generally southwest to northeast 329-km altitude circular orbit that passed almost directly over USAF's AMOS (Air Force Maui [HI] Optical Station [13]) observatory several minutes before local dawn. The zenith, solar-scattering, and aspect angles of the trail and its range from AMOS are shown in Fig. 4.

Discovery came into sunlight at 28 zenith, 248 azimuth at 15:21:59 UT (04:58 local time at AMOS), when the solar depression at its nadir was 19. The shadow height below the spacecraft trajectory decreased to about 100 km when the zenith angle increased to 67 (now in the northeast) some 2 min later. When direct illumination from the solar disk is limited to these high atmospheric altitudes, nightglow chemiluminescence and celestial sources are the principal optical background at the wavelengths to which the AMOS video camera responds; as we will show, this sky radiance was below the noise threshold of this camera. A few discrete

Fig. 2. View of the ice particle trail from *Discovery's* crew cabin (a) and in a space-simulation chamber [9] (b). The venting nozzle is about 5 m from the nearest segment of the beam that shows through the spacecraft window. The decrease in mean exposure with distance outward is due principally to the (1 distance)² decrease in irradiance from individual large particles. In (b) the scale at the particle stream is about 1 10; nozzle orifice diameter 3 mm, stream velocity 9 m s, temperature 20 C (illumination geometry unstated).

coordinates. A mission specialist held and pointed one of the low light level video cameras of shuttle's closed circuit T.V. system [12] through this window toward the particle trail [refer to Table 1 and Fig. 2(a)]. A second such operations-documenting room camera mounted in the cargo bay 17 m aft of the nozzle, remotely operated by a flight crew member viewing its display monitor, provided a projection of the sunlit water cloud (Fig. 1) about perpendicular to the more restricted and less readily interpretable
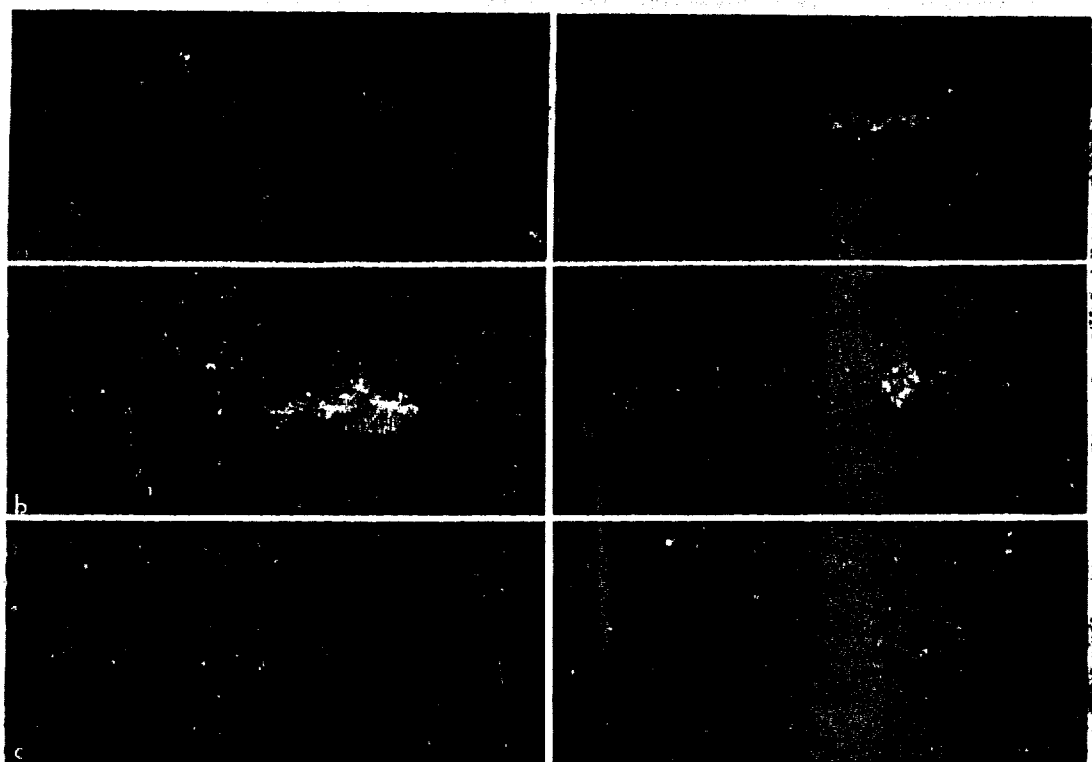
Fig. 3. Views of the sunlight-scattering trail from the AMOS telescope. with 0.8 of its 0.40°-horizontal image field reproduced. (a) At 15:22:19, zenith angle η_1 5.4°, range 331 km. (b) 15:22:23 (culmination), 1.5°, 330 km. visual magnitude of *Discovery* -0.2. (c) 15:23:40 (Figs 5, 6, 7), 61°, 637 km, $+3.6$, (d) 15:24:20, 72°, 891 km. (e) 15:25:40, 83°, 1432 km, $+5.6$. (f) 15:26:00, 85°, 1570 km. The video gain setting in general differs among images. The solar-scattering and aspect angles of these frames can be found in Fig. 4.

ground lights appear in the aft onboard camera's views into the nadir hemisphere, as would be expected from *Discovery*'s trajectory over the Hawaiian Islands. While stars are not identifiable in the onboard images, stars with visual magnitude up to about 11 can be seen moving across the narrow field of the 55 cm-aperture, further intensified (and thus very high irradiance sensitivity) AMOS camera.

We have derived the radii and sublimation rates of the recondensation ice particles from the radiance distributions in these groundbased photographs

(Section 5.2 and Appendix A), and estimated the fraction of the vented water in these smaller droplets and the mean radii of the very much larger ice droplets by considering also the irradiances that these latter particles produce in the onboard images (Sections 5 and 6).

3.1. Stationarity of the water venting

The discharge of supply water from the spacecraft may be considered a time-stationary event over the

Table 1. Video camera parameters

Location	Field of view	Axis pointing	Photo-cathode[d]	Brightness response	Solar angle	Background scene	Typical images
Payload bay, forward of Vertical Stabilizer[a]	Zoom, 47° horizontal in Fig. 1	Manual, by crew in el/az/ zoom	SIT, RCA 4804H type	Auto-ranging	~90–250	Ocean surface (clouds)	Figs 1, 8
Crew cabin window W1[b]	Zoom, about 45 in Fig. 2(a)	Handheld by Mission Specialist	SIT, RCA 4804H type	Auto-ranging	~130–230	Atmosphere limb in anti-solar direction	Fig 2
At AMOS,[c] 21 N—204 E, 3000 m altitude	0.40 × 0.30	Automatic, tracking on *Discovery*	ISIT, RCA 4849H type	Ground-based operator control	η_1 in Fig. 4	Night sky, at zenith angle η_1 in Fig. 4	Figs 3, 5, 6, 7

[a]Orbiter Station 1290, −x7, 446.
[b]Station 500, −60, 460.
[c]Air Force Maui Optical Station, Mt Haleakala, HI. 55 cm-diameter finder telescope, f 3.5, tracking jitter $< \pm 2$ pixels.
[d]S-20R, nominal FWHM photon response (uncorrected for telescope absorption) 0.37–0.68 μm. (I)SIT = (Intensified) Silicon Intensifier Target.

data period, in view of its venting and external geophysical conditions.

(1) The *flow rate* and *angle to the vehicle velocity vector* remain constant.

(2) The *geophysical parameters* that determine the heat balance of the ice particles remain essentially fixed over the relatively narrow range of latitudes and longitudes of the (constant-altitude) trajectory. (a) The change in solar irradiance due to in- and out-scattering of direct sunlight by the atmosphere is small (the full disk of the sun at tangent altitudes above at least 40 km illuminated the trail). (b) Changes in the thermal earthshine that might result from solar heating near dawn are less than the uncertainty in the flux of this infrared radiation at the particles. (As the heating effect of collisions is negligible at all expected air densities, changes in the ambient density need not be considered.)

Thus the montage in Fig. 3 represents a series of projections to the ground station of the same physical phenomenon, in which the viewing conditions—or "scene lighting"—change as follows over the ~5-min data period.

(3) The *scattering of solar photons* towards the camera from individual ice particles varies with the angle η_1 between the sun and line of sight (in Fig. 4). This dependence differs substantially between the two particle sizes (refer to Fig. 9), and thus plays a part in interpretation of the groundbased images.

(4) The *sight paths* through the quasi-conical, optically-thin cloud, and therefore its apparent surface radiances, vary as (sin[aspect angle η_2 of its symmetry axis])$^{-1}$ when $\eta_2 > \sim 10°$.

(5) The *plate scale* at the spacecraft is proportional to (range from AMOS)$^{-1}$.

(6) The *extinction* by the atmosphere above AMOS increases with zenith angle η_3. (As noted, the signal from the sky background, which also depends on η_3, is substantially less than the dark current.) LOWTRAN [14] calculations showed that the average transmission over the camera's wavelength sensitivity band of the near-Rayleigh nighttime
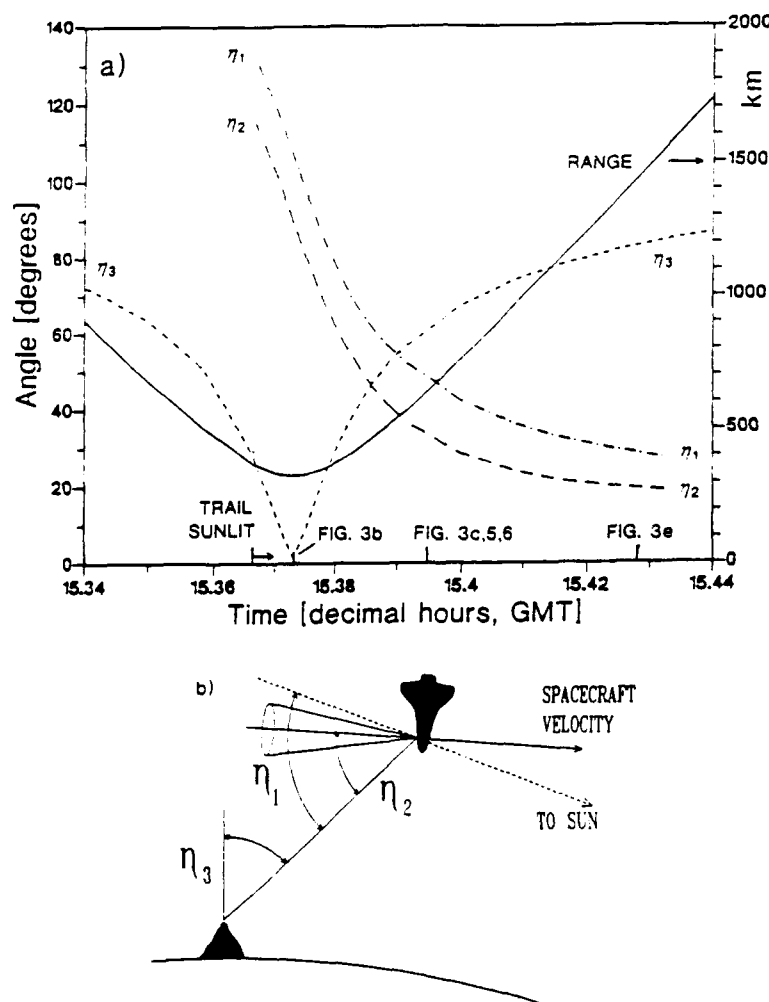

Fig. 4. (a) Solar scatter angle η_1, aspect angle to trail axis η_2, zenith angle of *Discovery* and trail η_3, and slant range to *Discovery* from AMOS (solid line) during the water venting. (b) Schematic of the viewing geometry from the ground station identifying the three angles.

atmospheres typically encountered at the mountain-top station is 0.85 in the zenith, decreasing to 0.7 at $\eta_3 = 61$ [Fig. 3(c)] and 0.25 at 83 [Fig. 3(e)].

In view of this physical stationarity, photometric-photogrammetric analysis of a single AMOS video frame would provide sufficient information about the mean radii and concentrations of the sunlight-scattering particles responsible for the optical signal at the groundbased camera. The dependence of the brightness of the trail on solar scattering angle η_1 as Discovery moves across the sky—"nephelometry", so to speak—further serves to identify the type of ice particle dominating the signal.

3.2. Operation of the video cameras

3.2.1. At AMOS. The electronic gain of the groundbased camera [13] (refer to Table 1) was man-ually changed several times over the exposure sequence in Fig. 3, with the operator applying the condition that its video amplifiers not be severely overdriven by sunlight scattered from Discovery's body—the bloomed area at the right of the water-particle trail—while the spatially-continuous image remained above noise on his display monitor. Track-ing jitter was so small as to be visually undetectable, and thus introduces negligible photogrammetric error when successive frames (in which the aspect angle of the trail is changing slowly) are coadded to improve the photometric signal noise ratios. We averaged 15 neighboring frames at the solar-scatter and aspect angle at which video data were analyzed in detail by first transcribing the standard broadcast analog video record to VHS format, and then digitizing to a 512×512 pixel, 8-bit gray scale stored as a binary disk file.

The brightness of the moonless night sky at 60 zenith angle over the S-20R spectral range is about 6000 rayleighs, or 10^{-10} w cm^2 sr. Manufacturer's specifications indicate that the resulting illumination of the cathode of the ISIT video receiver tube at the f 3.5 aperature ratio of the telescope-camera would produce photocurrents smaller than the dark current. This baseline pixel current averages 61 of 256 digitiz-ation units in the video frames that we selected for analysis.

Quantification of the scene brightnesses from the video signals requires a known relation between the experiment observable output current and input irradiance at the camera's image plane, to which this scene radiance—the physical quantity of interest—is proportional. The performance specifications for ISITs further state that near the dark-current baseline the incremental currents are directly proportional to the incremental irradiances (as would be expected: ISITs count photons much like electron multiplier-based phototubes), and that the slope of this response characteristic decreases as saturation output current is approached. (The effect of changing the electronic amplification of the AMOS camera is to change

its initial response proportionality factor or "con-trast", and concurrently its dynamic range; in prac-tice, the noise-equivalent irradiance usually depends on video gain.) We therefore adopt a linear relation-ship between the photocurrents-above-baseline and the visible radiances of the water-particle trail, with the recognition that the error in these radiances increases as current saturation (256 digitization units) is approached.

3.2.2. Onboard Discovery. The images from onboard the spacecraft, although also radiometri-cally uncalibrated, provide useful data on the number, longitudinal velocity (Section 4), and—qualitatively—irradiances of the individual ~milli-meter ice particles relative to those from the cloud of unresolved submicron particles. These somewhat less sensitive space shuttle cameras [12] have object position-sensing automatic control of their electronic gain and lens iris setting that provides very wide inter-scene dynamic range while protecting against overcompensation when very bright objects (such as Orbiter's sunlit bay) lie near the edge of their field of view. Like the AMOS camera, they operate at standard broadcast video (EIA RS-170) frame rates.

The southwestward-flowing (relative to Discovery) particle stream lies in the hemisphere away from the rising sun, and the scattering intensities toward these onboard cameras vary along the trail in each video frame: refer to Fig. 9. (In the much smaller-format groundbased images, they in effect vary only along the spacecraft trajectory.) The handheld crew-cabin camera views an about 20- to 200-m long segment of the flow path (depending on where it is pointed), while the azimuth and focal length settings of the payload-bay camera allowed it to view the vanishing point of the trail [Fig. 1(c)].

4. OVERVIEW OF THE IMAGE DATA

4.1. AMOS

The very high irradiances at AMOS due to scatter-ing of sunlight from Orbiter's high-albedo body result in the blooming of and undershoot in the spacecraft's image evident in Fig. 3. Irradiance from the vehicle is expressed by NASA as an equivalent stellar visual magnitude after a (nominal) correction for extinction by the intervening atmosphere. Typical such magni-tudes in the caption of Fig. 3, from the listing provided by Johnson Space Center, illustrate the very high sensitivity of the telescope-camera to spatially unresolved ("point") light sources.

The aforementioned changes along the trajectory in the relative photocurrent-to-irradiance response of the camera system are evident in the videotape. Hence the apparent brightnesses in the reproductions in Fig. 3 (the originals of which were made by photo-graphing single captured frames displayed on a video monitor screen at a fixed exposure time) would not accurately represent the actual time history of surface

brightnesses of the trail. The variability in apparent length of the sunlight-scattering volume above that due to the changing plate scale, aspect angle, and solar-scatter angle is also an effect of camera threshold. As Fig. 3 shows, the area of water trail above the noise level of the AMOS camera remains within its field of view over the period in which the trail is in sunlight.

The images at 15:23:40½–41 [one of which is Fig. 3(c)] show particularly good contrast due to their combination of small--i.e. "forward"—scatter angle η_1 (48°); relatively small aspect angle η_2 (33½°), so that the sight path length is about twice that in perpendicular projections); and long range to Discovery (NASA stellar magnitude $+3\frac{1}{2}$). (The resulting low irradiance from the spacecraft's body allowed the operator to enhance the extended source by increasing the electronic gain of the camera.) Although the about-normal projections when Discovery passes almost directly over AMOS are more geometrically favored than this view at 61° zenith angle, the contrast and area-above-threshold of the particle trail are substantially lower. We selected the projection illustrated in Fig. 3(c) for digital processing and analysis.

Figure 5 is a contour plot of the photocurrents from individual pixels averaged over 15 successive 1 30-s video frames. Fig. 6(a) is a longitudinal (long-axis) one-dimensional trace from this scene corrected for the foreshortening and sight path of its aspect angle, and Fig. 7 shows traces transverse to this axis at three distances from Discovery. Some effect of blooming from the spacecraft image and saturation

of the photocathode extends out to about 600 m. Extinction by a clear maritime (LOWTRAN [14]) atmosphere at the 61° zenith angle results in a small shift toward the red of the FWHM points of the product (atmosphere transmission)·(solar spectral irradiance)·(camera response), a parameter that we apply later in analyzing this image; see Fig. 10. We stress again that the distributions in space (relative to the moving spacecraft) and size of the two types of ice particle remain the same during the water-venting period: this particular two-dimensional projection of the three-dimensional volume scattering rates is judged to have the best signal-noise ratios for quantifying the pattern.

4.2. Onboard

The principal qualitative impression from playbacks of the videotapes from the onboard camera is of a spatially-dense stream of discrete particles with a relatively broad size distribution—as evidenced by the substantial differences among the irradiances from particles at fixed ranges—, each of which is moving away from the spacecraft at sensibly the same constant speed. While physical structure on these expectedly mm-diameter droplets is of course far below the lateral spatial resolution limit of these cameras at the distances to the trail, some particles appear to flicker (with roughly ½s periods). This modulation of their irradiances at the cameras shows that these are tumbling irregular ice water such as was seen in a laboratory simulation [8], rather than spherical liquid (or even solid) drops.
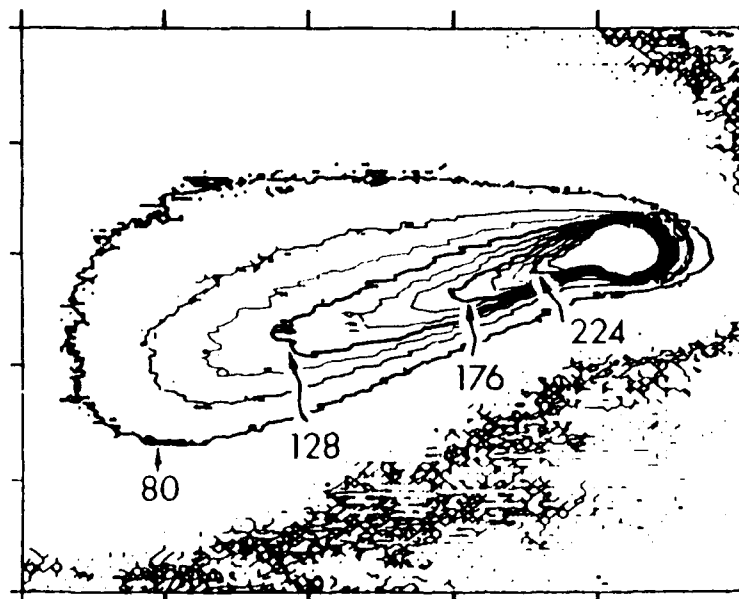

Fig. 5. Equi-photocurrent plot of the groundbased images centered on Fig. 3(c). with the contours separated by 16 of 256 digitization units. In the initial ~600 m of trail contamination by blooming from Discovery's body (NASA equivalent stellar magnitude 3.6), and photocurrent saturation effects, are present. The glow ahead of the spacecraft is an instrumental effect (of an overshoot that follows the undershoot). This plot is the basis of Figs 6 and 7.
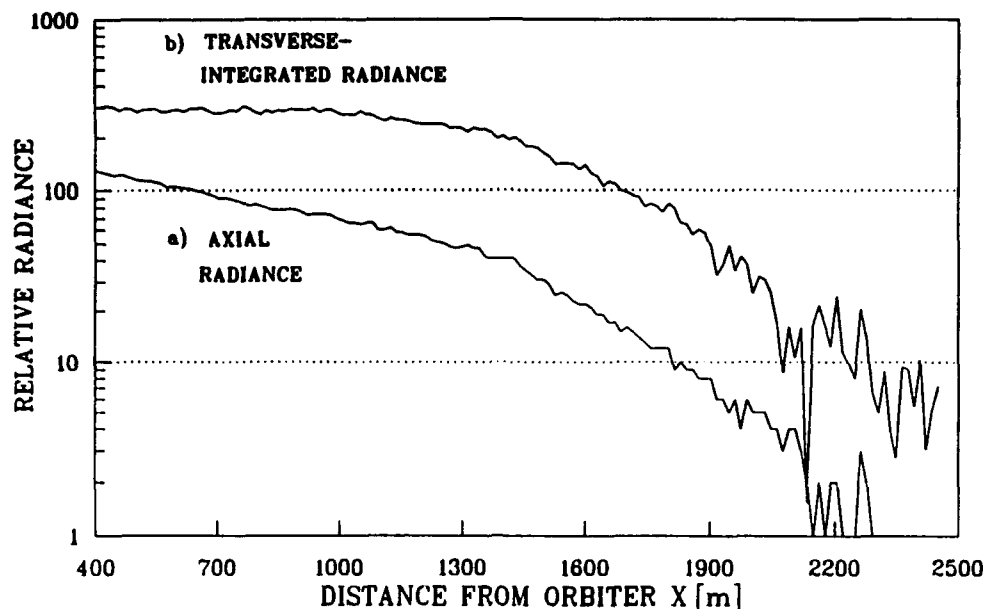
Fig. 6. (a) Relative radiance along the line of maximum brightness extending out from *Discovery* in Fig. 5, with the average baseline subtracted and a linear relationship between the video photocurrent and scene radiance assumed. (b) Radiances summed along lines transverse to this long axis (sterance per unit path).

Further evidence that the phenomenology of the vented water stream is at least qualitatively similar to that in the space-tank experiments comes from the comparison in Fig. 2 of a typical crew-cabin image with a laboratory photograph [9] of an injection of pure water with temperature 20 C, velocity 9 m/s, and nozzle diameter 3 mm (the illumination conditions were not specified).

The spatial density of these particles, counted from the bay camera images (in which absolute distance scales can be determined), is 100 ± 50 per meter of longitudinal path. This density is consistent with the mass flow rate and expected mean particle size (a point to which we return later). The angular divergence of the radiation pattern seen from *Discovery's* two camera positions indicates that its apex is within a very few m from the nozzle, perhaps even within a few 10's cm. The half-angular spread, ~10°, is sensibly the same in the two about-perpendicular onboard projections, and furthermore is experimentally indistinguishable from the divergence of the trail in the groundbased images. The transversely-directed kinetic energy imparted to the droplets as the stream bursts is of the order of 10^{-3} J/g, which is very
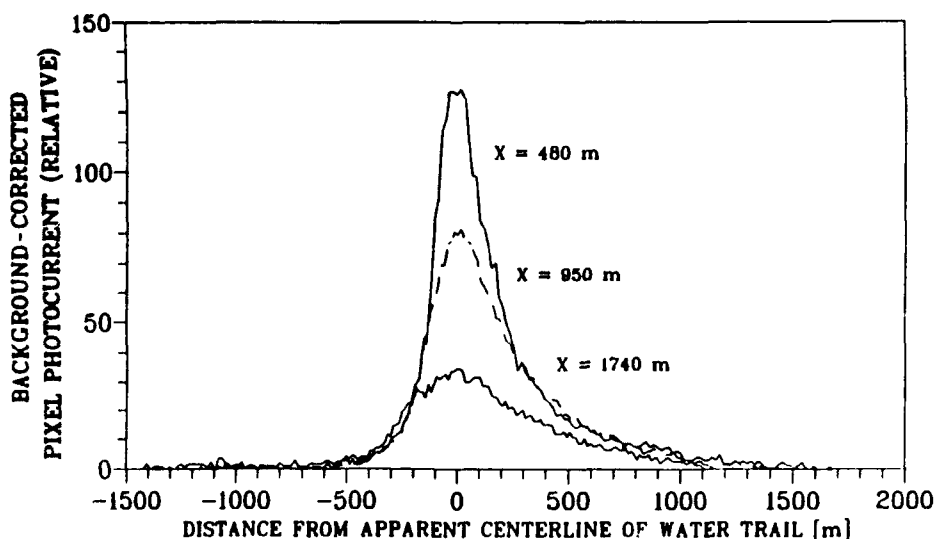

Fig. 7. Relative radiances along lines transverse to the long axis of the trail in Fig. 5 at the downstream distances X indicated. The decrease in area under these radiance plots (Fig. 6b) indicates qualitatively that the radii of the ice particles are decreasing with increasing X.

small compared with the ensuing changes in their heat content (see Appendix B).

The instrumentally bloomed images of these many discrete large ice particles produce a spatially continuous overlay of apparent brightness, which can not be distinguished from the radiance that would result from scattering of sunlight from an accompanying cloud of unresolved small (recondensation) particles. (Indeed, some of the image-plane irradiances are so high that they produce the undershoots along the scan direction characteristic of intensified video cameras.) As Figs 1 and 2 show, this "haze" does not

extend beyond the distinguishable particles in the direction perpendicular to the long axis of the trail, which indicates that if this apparently-continuous signal is due in substantial part to the small particles their transverse velocities would be about the same as those of the large particles. We return to this important issue in Section 6.

4.2.1. Payload bay. When part of *Discovery's* sunlit cargo bay is in the field of view of the aft camera [as in Fig. 1(a)] its video gain decreases, reducing the photocurrents from the trail. The low surface brightnesses within the first few m from the
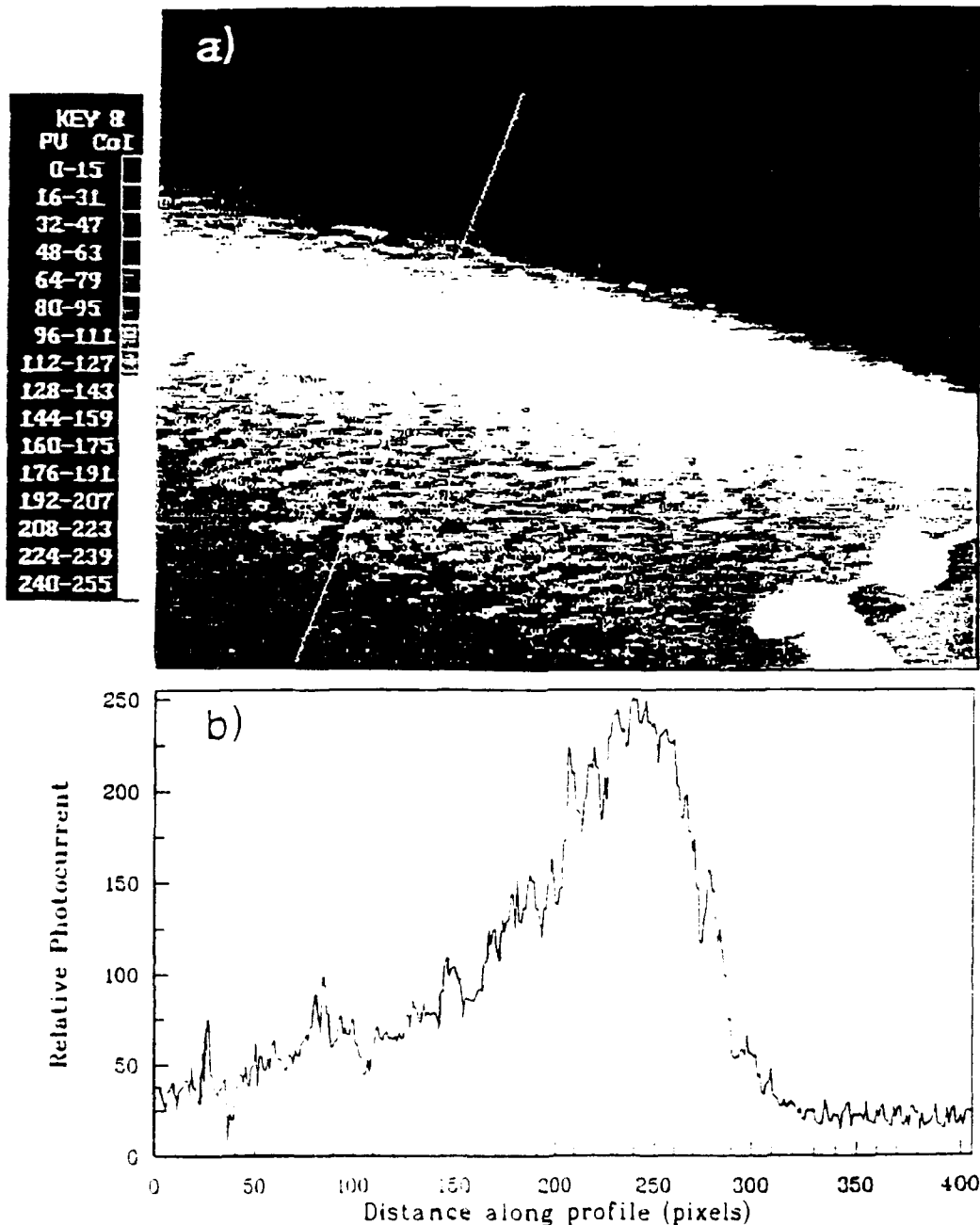

Fig. 8. (a) Equi-photocurrent plot of the water trail from the aft (payload bay) video camera [Fig. 1(b)]: the horizontal angular field is about 48. (b) Profile across this image along the diagonal line shown.

nozzle are most probably due to shadowing of the particle cloud by the spacecraft body, as the sun is on its opposite side. We interpret the bright region to the right of center in Fig. 1(b) as a rainbow, that is, as the about order-of-magnitude increase near 137° scattering angle in the differential scattering cross-sections of spherical ice (or water) droplets whose diameter is large compared with the light wavelength; refer to Fig. 9. Figure 8 is an equi-photocurrent contour plot of Fig. 1(b) with the high spatial frequencies from the individual particles filtered out, and a transverse trace at about 28 m downstream from the spacecraft. The asymmetry in brightness, with the steeper edge toward the earth, is seen also in the groundbased images (Fig. 3); this effect may be due to imperfections in the water-venting orifice.

In Fig. 1(b) the generally-smaller aspect angles of the trail increase the slight pathlengths and thus the mean radiances. In Fig. 1(c) the bay camera is pointing at a still larger azimuth angle from Orbiter, so that the still shallower mean aspects further increase the projected brightnesses. The vanishing point of the wake trail is within the field of view in these latter camera frames.

4.2.2. Velocity of the large ice particles. We measured the longitudinal speeds of identifiable sunlight-scattering particles from their positions in successive video frames from this aft video zoom camera [as in Fig. 1(b)]. (The handheld crew-cabin camera lacks a useful geometric reference.) This camera views to within 14 from perpendicular to the symmetry axis of the trail, where the particles emerge from behind *Discovery's* open bay door. We determined the horizontal field of view of the camera at the time of the velocity measurements from the angle subtended by a radiator panel mounted along this door, which we identified on scale drawings of Shuttle Orbiter. This object measures 1.5 m transverse to its direction to the bay camera, from which it is on average 9.6 m distant, and its image extends across 0.19 of the video frame. These dimensions would result from a full horizontal angular field of 47½, with an uncertainty that we estimate as ±7.

We advanced the videotape successively one full 1 30-s frame, recording the number of frames during which identifiable particles moved from 27 from the nozzle to 39, which r presents a pathlength of 7.7 m. (Efforts to time the movement across the full horizontal camera field produced less reliable results due to the error in assigning a longitudinal distance traveled.) In 7 trials on high-irradiance droplets moving within 5 of the long axis of the trail the number of video frames per such transit was 10, with a standard deviation of less than 1 (fractional frames could be estimated). This small spread indicates that these large particles have a narrow longitudinal velocity distribution, as would result if the speeds imparted to them in the fragmentation of the

initially-liquid stream were principally transverse-directed.

The mean speed along the trail axis measured by this procedure was 23 m/s. Taking into account the systematic errors in timing the transits and in the full and partial fields of view of the bay camera at the particle trajectories, we estimate the uncertainty of this measurement to be +25%, −35% (or +6, −8 m/s).

This velocity in free space can be compared with the velocity derived assuming fully developed Poiseuille flow in the conical nozzle, which is [7] 1.32 (volume vented per unit time) (exit cross sectional area) = 16 m/s. The condition for achieving this free-stream velocity is that the Reynolds number in the nozzle (essentially, [flow velocity] [diameter] [viscosity]) be greater than about 100 [7]. The parameters for *Discovery's* venting place the Reynolds number much higher: the numerator in this expression is about 100 g/cm s, while the viscosity of 30°C water is 0.008 g/cm s. The ejected liquid stream contracts to (0.87) (1.4 mm) = 1.2 mm as its radial velocity profile relaxes to uniform from parabolic (i.e. Poiseuille) just beyond the venting orifice, with the average speed increasing by 32%. As the later cavitational breakup would not impart a net longitudinal velocity to the product droplets, we conclude that the particle velocity measured above is consistent within its relatively large error with steady Poiseuille flow in the nozzle followed by relaxation to a radially-uniform flow velocity distribution in the liquid stream before it breaks up.

5. PHOTOMETRIC ANALYSIS OF THE AMOS VIDEO IMAGES

We show next that the radiances measured in the projection to the ground station (Fig. 3) are due principally to the submicron-diameter recondensation ice droplets, and that the rate of decrease of sunlight scattering cross-section of these particles is consistent with standard radiation theory when a physical plausible correction is applied for the change in their absorption/emission—and therefore sublimation rates—as their surfaces roughen. We then estimate the sizes and abundances of both the millimeter and submicron particles from the relative image irradiances that each flow component produces at the distant and close-lying cameras. The detailed calculations of the radius and temperature of the two types of particle are in Appendices A and B.

5.1. Velocity of the condensate ice particles

A calculation of the spatial distribution of these small particles would involve the trajectories of the explosion-product droplets, since as these droplets are formed while the mean temperature of the liquid stream is still high (so that the vaporization rate

remains high) they would be the source of most of the gaseous water. (Our estimate in Appendix B of the fraction from the bundled stream is 5%.) The mean directed velocity of the expanding water gas evaporated/sublimed from each drop is the same as that of the drop itself. Since the submicron particles by definition form where the water vapor is collisional rather than supersonic—that is. where the gas velocities are randomized in a reference frame of the drop(s)—the distribution of transverse velocities of these condensate ice particles would be the same as that of the large water ice particles.

As we found in Section 4. the photographs from onboard *Discovery* do not show any evidence of an unresolved sunlight-scattering volume having a different angular speed from that of the cloud of readily-distinguishable. polydisperse large ice drops. (The "haze" underlying the individual high irradiance patches may in any case be due to video blooming.) The observation that the angular extents of this large-particle trail close to the spacecraft and the longer wake trail of recondensation particles in the AMOS images are the same within the error of interpretation of the exposure patterns. provides further evidence that the mean velocities of the two particulate components are sensibly the same.

Further, we identify no physical process that imparts a directed longitudinal velocity to the small particles relative to the large particles. (Drag from collisions with the atmospheric gas has negligible separating effect at *Discovery*'s orbital altitude.) In

view of these findings we conclude that the small ice particles move with these much larger water/ice droplets. a result applied in calculating the sublimation rates per unit downstream distance (in Appendix A).

5.2. Radiance pattern

For the reasons presented in Section 4.1. we focus the radiometric analysis on the 0.5 s-averaged video frames centered on Fig. 3(c) and shown in radiance contour form in Fig. 5. from which follow the plots of baseline-subtracted axial brightness and transvere-summed brightness per unit trail length of Fig. 6(a) and (b). This latter quantity—sterance per unit flow path. sometimes referred to as station radiance—. is the area underneath the curves of brightness perpendicular to the trail axis in Fig. 7. As it eliminates the effect on surface radiance of the divergence of the flow. this quantity is a quantitative measure of the cross-sections of the particles for scattering visible sunlight in the direction of the AMOS camera.

The critical qualitative feature of Figs 6(b) and 7 is the large decrease in this spatially-integrated surface radiance with distance from *Discovery*'s venting nozzle (after the region where video blooming and nonlinear response are significant). This immediately shows that the particles principally responsible for the signal at AMOS lose a substantial fraction of their optical cross-section—which is to say. volume—
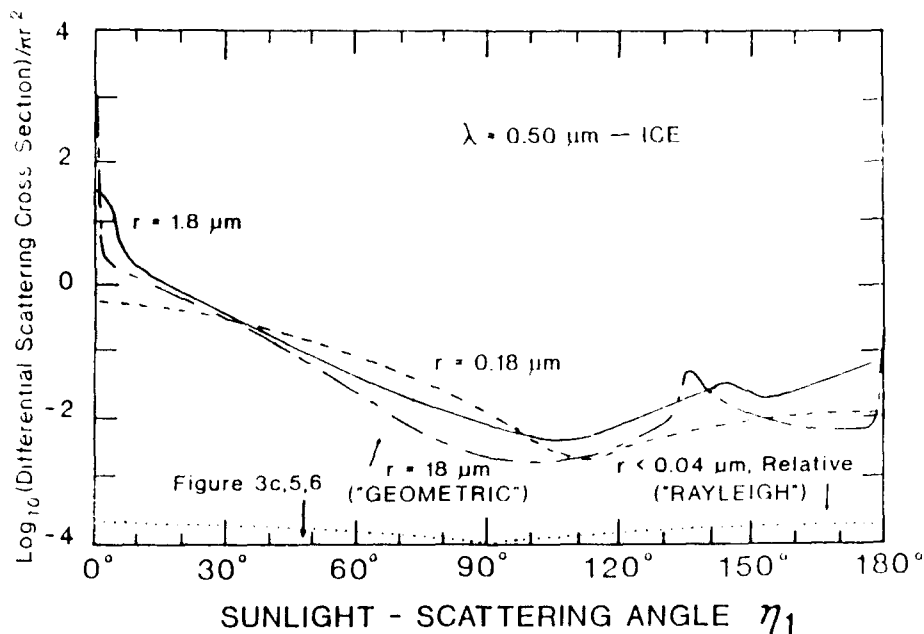

Fig. 9. Phase functions of "Rayleigh" ($< \sim 0.04\,\mu$m. relative). $0.18\,\mu$m. $1.8\,\mu$m. and $18\,\mu$m radius spherical 266 K ice particles under $0.50\,\mu$m illumination (average of both polarizations). The factor ~ 2 amplitude Mie oscillations for the larger-radii particles are suppressed. as this small-scale variability is damped by the $\sim 0.25\,\mu$m range of wavelengths of illumination and detection in the AMOS images (Fig. 10). The results for $r = 18\,\mu$m are valid to within a factor 1 1 2 for radius $r > \sim 10\,\mu$m. and thus apply to spherical stream-fragmentation droplets.

within the trail's instrumentally-detectable $\sim 2\frac{1}{2}$-km length. The mm-diameter water/ice droplets would lose only about 15% of their mean cross-sectional area in the < 2-min transit time beyond the bloomed pixels (see Appendix B), and therefore could not account for the almost two orders of magnitude decreases in sterance per unit path actually observed. In constrast, such a large change would result from the sublimation from the much smaller recondensation ice particles (Appendix A).

5.2.1. Dependence on solar-scatter angle. This conclusion is supported by the dependence of the visible radiances of the wake trail at fixed downstream distances on the sunlight-scattering angle η_1. This angle decreases from 90 16s after Fig. 3(b) (before which excessive blooming of the images of the spacecraft body at its relatively short ranges from AMOS precludes even a qualitative estimation of the cloud brightnesses), to about 30° in Fig. 3(e) 3 min later. Despite the effect on the optical signal of the electronic gain changes made over this trajectory segment, the increases in radiance at fixed distances along the trail (corrected for the sight-path length) can be estimated as at most only one order of magnitude. Such a variation is consistent with "near-Rayleigh" or Rayleigh scattering (where 2π [particle radius r]/[mean photon wavelength $\bar{\lambda}$] $< \sim 3$), that is, by spheres whose radius is less than about $1\cdot4\,\mu$m; refer to Fig. 9. (In the Rayleigh regime the change would be $[1 + \cos^2 30]$, or less than a factor of two.) "Geometric" scattering ($2\pi r/\bar{\lambda} \gg 1$), by the mm-diameter particles, would in contrast result in brightness increases of about two orders of magnitude over this range of solar-scatter angles.

5.2.2. Particle radii and temperatures. A substantial change i the mean logarithmic slope of the radiances appears to be taking place about halfway along the particle trajectory in Fig. 6. The most

obvious physical explanation [1] of this sharply increased rate of brightness decrease is that the particles are undergoing a transition from the geometric sunlight scattering regime, where their differential cross sections vary about as r^2, into the Rayleigh regime, where these cross sections change much more rapidly with radius—specifically, with r^6.

In Appendix A we calculate the dependence on time-after-formation or downstream distance Y of (1) r and the temperature T of these ice particles and (2) the transverse-summed relative radiances of a wake trail composed of a monodisperse ensemble with (submicron, transitioning) r. For (1) we applied the rate eqn (A1) [15,16] that relates the heat the particles lose by bulk cooling, thermal gray-body emission, and (particularly) sublimation to the heat they gain from absorption of solar radiation and (primarily) infrared earthshine. A second relationship between the two unknowns is provided by the dependence on temperature of the sublimation rate from spheres whose radius is less than the mean free path of the evolved gas immediately off their surface [7]—so that little redeposition occurs, a condition that applies beyond a few m from the venting nozzle— $|dr/dt| \sim$ (equilibrium vapor pressure at T)/$T^{1\cdot2}$.

In an initial such calculation we made the implicit assumption that these particles remain smooth-surfaced spheres with emissivities/absorptivities derivable from the complex index of refraction of ice [17] by standard Mie theory [18]. We determined their effective cross-sections for scattering of visible sunlight by first computing the "wavelength response" of the experiment's system of illumination and photon detection, the product [solar spectral irradiance] [transmission of the atmosphere above AMOS] [relative sensitivity of the photocathode of the telescope-camera], which is plotted in Fig. 10. A model clear maritime atmosphere in LOWTRAN [14] was
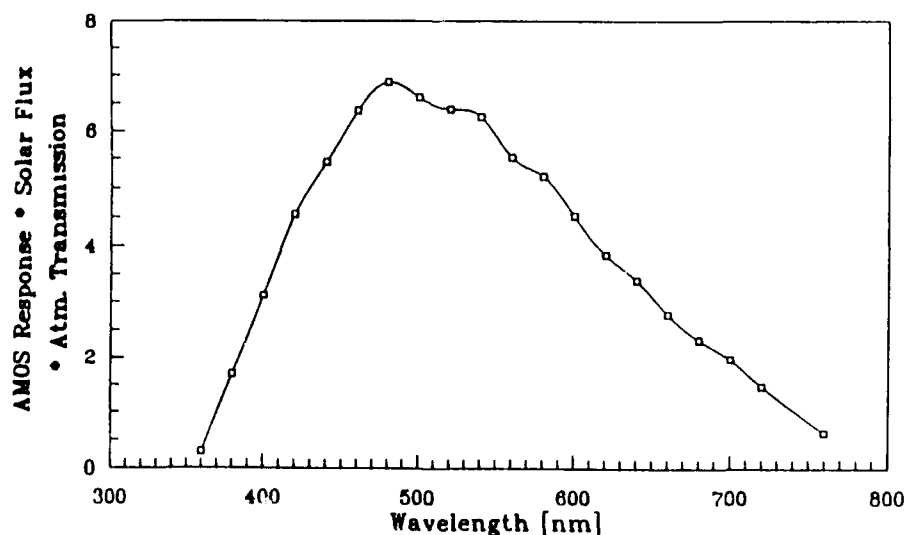

Fig. 10. Product of (AMOS camera response) · (atmospheric transmission) · (solar spectral irradiance), in relative units (see text).

used in deriving the transmissions along the $\eta_3 = 61^\circ$ sight path (which in practice has about the same spectral shape as that of a pure Rayleigh atmosphere), and the manufacturer's data on the relative quantum yield of S-20R ISITs of the type used in the groundbased sensor were adopted (which may introduce some error at the shorter wavelengths in Fig. 10 due to neglect of absorption by its glass optical elements). We next computed the differential scattering or phase function [18]—cross-section per unit projected area πr^2 for scattering photons into unit solid angle at η_1—of ice spheres with radius between 0.05 and 0.5 μm at wavelengths between 0.4 and 0.7 μm, averaging between $\eta_1 = 46$ and 50 to minimize any artifacts from small-sca'~ Mie oscillations; and weighted them by the response factor in Fig. 10 to derive the effective phase functions near 48 shown in Fig. 11. As would be expected, this averaged scattering function is relatively flat at radii above about 1 4 μm (although it does evidence some of the overshoot characteristic of monochromatic illumination of monodisperse particles), and then fairs into the strictly Rayleigh region very near 0.15 μm (where $2\pi r \cdot \lambda$ is close to 2).

Since the constants of integration of the rate equations and the total number of vapor-recondensation particles are not known, a normalization of the results of the calculations in Appendix A to the measured crosswise-summed trail radiances is needed. The manual "best-fit" to the data from Fig. 6(b), plotted in Fig. A2, indicates that beyond $X \approx 1$ km the sunlight-scattering cross-sections are decreasing at a much higher rate than this standard energy-balance and Rayleigh–Mie scattering theory predicts. Increasing (or decreasing) the downstream velocity of the small particles does not improve the fit, nor does adoption of a spread of initial particle radii (which would result in upward

curvature of the log-radiances in Fig. 6, the opposite of that observed).

The difference between the measured and first-order theoretical rates of changes of radius is in the direction that would result from roughening of the surface of sublimating ice, a phenomenon seen in laboratory tank experiments with somewhat larger droplets [15]. In consequence we repeated the calculations with the effective emissivities (thermal and relating to absorption of earthshine and near-infrared sunlight) progressively changing with radius of the "aging" vacuum-exposed particles as described in Appendix A. A satisfactory fit to the AMOS radiance data (Fig. A2) was achieved with emissivity increases varying with the square root of the differences between the initial radius r_0 (whose best-fit value is 0.30 μm) and r, a behavior that would be expected from "random walk-like" irregular erosion of the droplet surfaces. The resulting radii and temperatures of the particles are compared to Fig. A1 with those that we initially calculated without this surface roughening. Note that the radii transition into the Rayleigh regime near 50 s $\approx$ 1 km flight path X, as expected [1] from Figs 6(b) and A2. Radii of the order derived result in "efficient" scattering of visible light from a fixed total mass of ice (or liquid water).

5.3. Absolute brightnesses

These radii and the column densities of the small particles estimated as described in Section 6.3 lead to an estimate of the absolute radiances of the (optically-thin) trail in the projection of Fig. 3(c). The rate at which these particles (denoted here by the subscript m) are produced is

$$(dN/dt)_m = (dM'/dt)f_m/(4\pi \cdot 3)r_0^3 \rho \qquad (1)$$
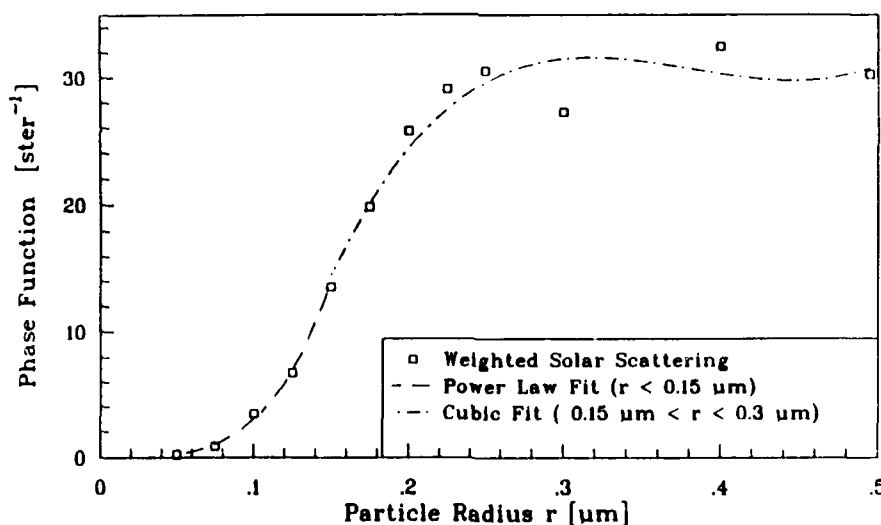

Fig. 11. Differential scattering (phase function) of ice particles averaged over $\eta_1 = 48^\circ \pm 2^\circ$ weighted by the system "response" factor in Fig. 10, in relative units.

where $dM'/dt(= 19.4 \, g/s)$ is the flow rate of the vented liquid stream, f_m is the fraction of this total mass that recondenses, $\rho(= 0.92 \, g/cm^3)$ is the density of ice at temperatures near 200 K, and r_0 is the best-fit initial mean radius of these droplets (0.3 μm) from Appendix A. Their number density $n'(X)$ at distance X from *Discovery*, with the simplification that it is constant out to half-angle θ ($\approx 10^\circ$ in the AMOS images), is closely

$$n'(X) = (dN/dt_m) \, \pi (X \tan \theta)^2 \cdot v \qquad (2)$$

where $v(\approx 23 \, m \, s)$ is the downstream velocity of the small particles relative to the spacecraft.

The volume V of the elliptical slab of sunlight-scattering droplets containing the line-of-sight from AMOS to the axial point at X is to a good approximation

$$V(X) \approx \pi (X \tan \theta) \cdot (X \sin \theta) \, \Delta X \qquad (3)$$

where ΔX is the longitudinal thickness of the slice of trail. The irradiance I_m at AMOS from V is

$$I_m \approx I_{sun}(dC_{sc}/d\Omega)_m n' V R^{-2} \qquad (4)$$

where I_{sun} is the solar irradiance within the spectral sensitivity of the camera ($\approx 4 \times 10^{-2} \, w \, cm^2$, taking into account the $\sim 15\%$ attenuation by the atmosphere above its mountaintop altitude), $(dC_{sc}/d\Omega)_m$ — the differential scattering cross-section—is πr^2 times the system-weighted photometric function of individual small particles at $\eta_1 = 48^\circ$, and $R(= 637 \, km)$ is

the range of the cloud from AMOS. The surface brightness $B_m(X)$ on the long axis of the trail is then

$$B_m \approx I_m R^2 (2X \tan \theta) \cdot (\Delta X \sin \eta_2) \qquad (5)$$

where $(2X \tan \theta) \cdot (\Delta X \sin \eta_2)$ is the area of volume $V(X)$ projected along the line of sight and η_2 is the view aspect angle $[=33\frac{1}{2}$ in Fig. 3(c)]. Substituting eqns (1)–(4) into eqn (5), we get

$$B_m \approx I_{sun}(dC_{sc}/d\Omega)_m f_m (dM'/dt) (4\pi/3)$$
$$\times r_0^3 \rho 2vX \sin \theta \sin \eta_2. \qquad (6)$$

At $X = 1$ km the radius of the small ice particles (assumed to remain spheres) has decreased to about 0.15 μm (Fig. A1), for which Mie scatter theory predicts $(dC_{sc}/d\Omega)_m = 5.7 \times 10^{-11} \, cm^2 \, sr^{-1}$ at 48°. Substitution of the numerical values gives

$$B_m(X = 1 \, km) \approx 9 \times 10^{-7} (f_m/1\%) \quad (w \, cm^2 \, sr). \qquad (7)$$

Figure 12 is a re-plot of the axial radiances of Fig. 6(a) on this "absolute" scale with f_m 1% taken as 2 (from its estimation in Section 6.3), with a comparison to (1) the radiances that would result from scattering of sunlight by stream-fragmentation ice particles with two mean diameters within the range expected and (2) the brightness of the moon-less $\sim 61^\circ$ zenith-angle night sky that we estimated in Section 3.2.1. Since the highest photocurrents
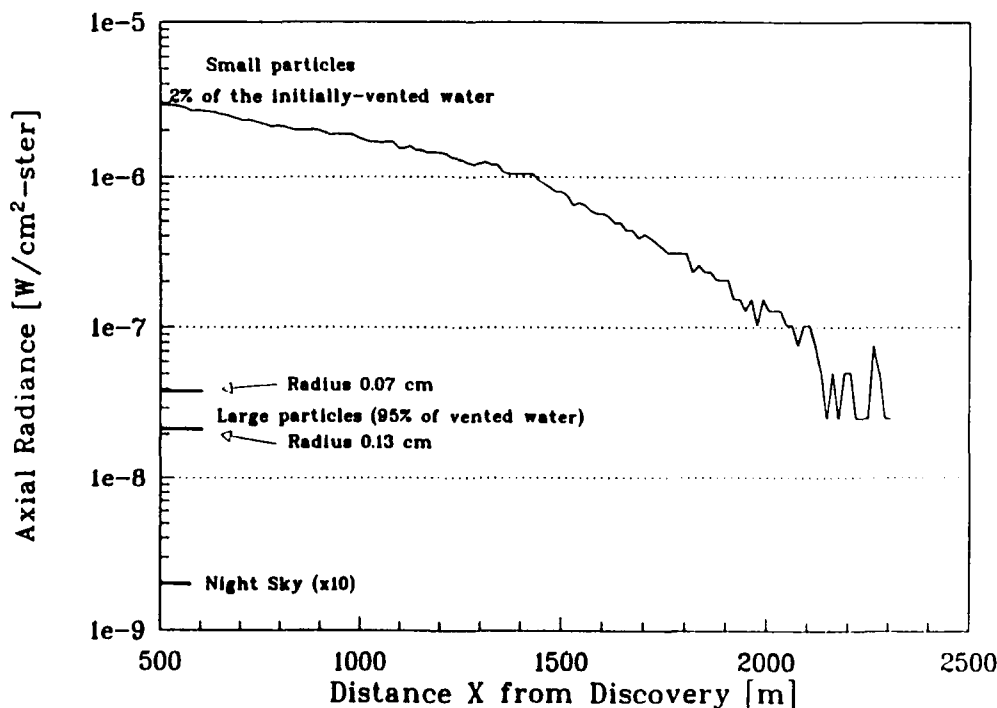

Fig. 12. Measured visible trail radiance on the absolute scale derived in Sections 5 and 6. The signal from the discrete large particles does not perturb the radiance distribution. The brightness of the night sky at 61° zenith angle is well below the noise limit of the AMOS camera.

produced by scattering from the wake trail are only about three times larger than those of the dc scene background in Fig. 3(c) (195 relative to 61 digitization units). Fig. 12 shows that this large baseline would be almost completely due to the dark current of the AMOS video camera (even were I_m as small as $1 \cdot 10^0$ o).

An expression analogous to eqn (6) applies to the surface brightnesses produced by the underlying cloud of large particles in the projection to AMOS. With their parameters identified by the subscript M, the ratio of radiances is

$$B_m \cdot B_M = (I_m \cdot I_M)(r_M \cdot r_m)^3$$
$$\cdot (dC_{sc} \cdot d\Omega)_m(X) \cdot (dC_{sc} \cdot d\Omega)_M \quad (8)$$

r_M and its cross-section represent averages over the broad distribution of particle sizes and aspect ratios). Equation (8) explicitly includes the dependence on λ of the sunlight scattering cross-section of the rapidly-sublimating small particles, while the corresponding term for the large particles remains about constant (as shown in Appendix B). In consequence the dependence of B_M on X reduces to the $1 \cdot X$ ($\equiv$ [sight path length X] ["beam" divergence X^2]) factor [compare eqn (6)], as is apparent in Fig. 12.

These dependences of radiance on downstream distance X, and the analysis in Appendix A (as well as the dependence on η_1 outlined in Section 5.2.1), present strong evidence that $B_m \cdot B_M$ is greater than 1 over the detectable wake trail. Since signal-to-noise in the summed video image of Fig. 5 deteriorates rapidly beyond about 2 km from *Discovery*, we adopt the bound

$$B_m \cdot B_M > 1 \quad (\text{at } X \leqslant 2 \text{ km}). \quad (9)$$

At this downstream distance $r = 0.10$ μm, for which $(dC_{sc} \cdot d\Omega)_m = 6.3 \times 10^{-12}$ cm^2 sr^{-1} at 48°. The corresponding $(dC_{sc} \cdot d\Omega)_M$ is $0.1 \pi r_M^2$ cm^2 sr^{-1} (Fig. 9). With the fraction f_M of the vented water mass remaining in these solidified and further-cooled large particles (0.75) and the other numerical values stated above, eqn (8) and (9) give (r_m is in cm)

$$B_m \cdot B_M = 670 f_m r_M \geqslant 1$$

[at $X < 2$ km in the AMOS image analyzed]. (10)

6. PHOTOMETRIC ANALYSIS OF THE ONBOARD-CAMERA IMAGES

As we have seen, discrete large water ice drops are the dominant feature in the frames from the close-lying onboard cameras (Figs 1, 2 and 8); and a spatially-continuous haze with sensibly the same transverse angular extent overlies their instrumentally-blurred image spots, some of which may be due to scattering of sunlight from the submicron particles with the remainder resulting from overlapping blooming. The relative irradiances produced by the two size particles in the video photographs from the distant and nearby cameras impose an experimentally-rough joint constraint on I_m and r_M, as I_m or $B_m \sim I_m$ in both cameras—radiances being independent of range—while the exposures produced by the large particles are proportional to r_M^3 in the onboard images (where individual such drops are resolved) and to $(r_M^3 \cdot r_M^3) = r_M^3$ in the groundbased images (where they are not: the cloud produces the optical signal).

6.1. Small particles

The camera parameters adopted for calculating the irradiances from scattering of direct sunlight from both size particles are lens focal length $F = 2$ cm (derived from the camera's apparent field of view and the 1 2-in. physical width of its photocathode [12]), clear aperture A (which cancels out when the ratio of irradiances is taken), and effective image blur spot $A' = 40 \mu$m $\times 40 \mu$m (typical of the area from which most of the photocurrent from point sources arises in intensified video receiver tubes). (The contribution to the illumination of the trail by solar photons diffusely reflected off *Discovery*'s body is small enough to be neglected.) Our conclusions are not particularly sensitive to these and the following numerical values.

The relevant scene-lighting parameters at distance into the wake $X \approx 8$ m are aspect angle $\eta_2 \approx 45°$ and sunlight scattering angle $\eta_1 \approx 140$ (we introduce the prime symbol here to identify the projection to this onboard camera). For small-particle radius $r = 0.3 \mu$m the differential visible-light scattering cross-section $(dC_{sc} \cdot d\Omega)_m$ is calculated (from the procedure resulting in Fig. 11) to be 2.2×10^{-11} cm^2 sr^{-1}. The irradiance produced at the focal plane of the camera by the cloud of submicron particles is

$$I_m = B_m A \cdot F^2 \quad (11)$$

with its surface brightness B_m' in the projection to onboard given by the equivalent of eqn (6). Substitution of the numerical values into eqn (11) gives

$$I_m = 1.1 \times 10^{-4} A f_m \quad (\text{w/cm}^2). \quad (12)$$

6.2. Large particles

As these distinguishable particles lie far outside the hyperfocal distance of the onboard camera's short focal length lens, their corresponding mean irradiance at the focal plane is

$$I_M = I_{sun}(dC_{sc} \cdot d\Omega)_M R'^{-2} A \cdot A'. \quad (13)$$

$(dC_{sc} \cdot d\Omega)_M = 3 \times 10^{-2} \pi r_M^2$ at $\eta_1 \approx 140$ (Fig. 9), and $R' \approx 10$ m is the range to the sunlight-scattering particles located at $X = 8$ m. These parameters give

$$I_M = 2.3 \times 10^{-4} A r_M^2 \quad (\text{w cm}^2). \quad (14)$$

Thus the ratio of image-plane irradiances from scattering of sunlight by the relatively-few discrete large particles (still approximating them as spherical) and by the optically-continuous cloud of many smaller particles is

$$I'_m \, I'_M = 0.45 f_m \, r^3_M < \sim 1 \quad (\text{at } X \approx 8 \text{ m}). \quad (15)$$

The quantitative statement of the observation that the large particles stand out clearly above the "haze" in these onboard images is that their individual irradiances are at least equal to that from this smooth feature, as stated in eqn (15).

6.3. Particle parameters

From the constraint expressed by the inequalities of eqns (10) and (15) and the number density of the distinguishable particles estimated from onboard images [such as Figs 1(a) and 2(a)], f_m and r_M can be estimated. Figure 13 shows what we may term the $f-r$ domain of the two-component cloud of ice droplets, which bounds these two quantities from the observed ratios of radiance in projections toward AMOS from $X > \sim 500$ m and of irradiance at Discovery's cabin camera from ~ 5 m $< X < \sim 40$ m.

The number of discrete scattering particles per unit length of trail is as noted previously 100 ± 50 m^{-1} (this approximate figure includes an allowance for particles obscured by overlap near the trail axis). With the known water venting rate $dM' dt$, mass fraction in stream-fragmentation particles f_M (near $X = 8$ m it is about 0.95, as

these droplets have undergone little evaporation; sublimation; see Appendix B), and measured velocity v, 100 particles m^{-1} gives $r_M = 0.13$ cm.

Applying this "mean" radius with the joint constraints illustrated in Fig. 13, we find $f_m = (2.2 \pm 0.7)\%$, which is within the range estimated in the laboratory work [10]. The stated error takes account only of the uncertainty in counting the number of large particles per unit length of wake trail; the total uncertainty in r_M (an average, and in fact not well defined) and f_m would be higher. Figure 13 nonetheless indicates that the image-irradiances from the groundbased and onboard video cameras force the $f-r$ domain to a small region: f_m and r_M take on a narrow range of values for $B_m \, B_M \approx 1$ and $I'_m \, I_M \approx 1$.

7. RADIATION AND SCATTERING AT OTHER WAVELENGTHS

Arguments similar to those above show that the infrared thermal emission from the few large particles exeeds that from the many submicron particles, which radiate and scatter inefficiently at wavelengths long compared with their circumference (their emissivities are of the order of 10^{-3}, even taking into account surface roughening). That is, in projections to distant sensors the ratio of brightnesses of the two components of the water venting cloud at IR wavelengths differs strongly from that from scattering of visible sunlight. Since the temperature of the large droplets becomes lower than that of the
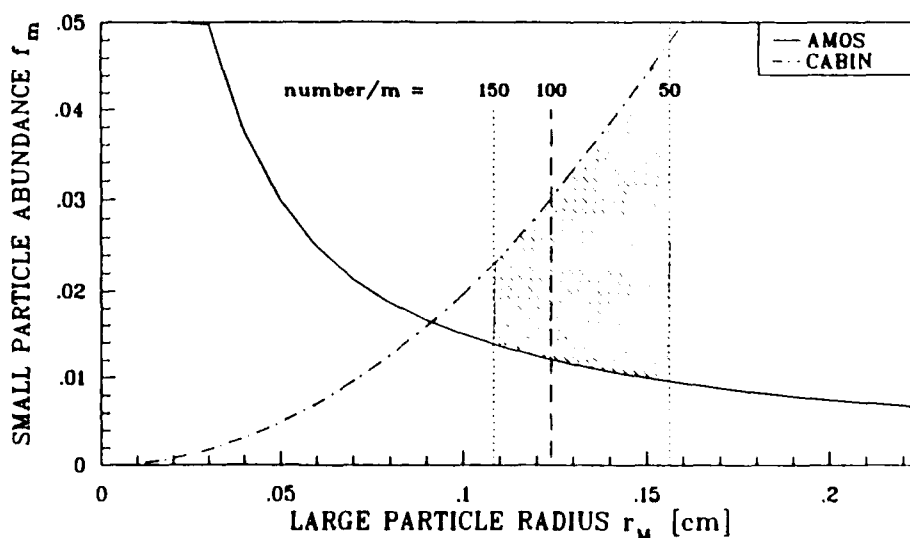

Fig. 13. Small particle abundance-large particle size ($f-r$) diagram of the water trail. The solid curve, which bounds $f_m > 1.5 \times 10^{-3} r_M^{-1}$ [eqn (10)], results from the observation that the signal at the groundbased camera is dominated by scattering of sunlight from the submicron ice particles (Fig. 12). The dot-dashed curve, which bounds $f_m < 2.2 r_M^3$ [eqn (15)], results from the observation that the $\sim$mm particles are prominent in the projection to the onboard camera. The mean large-particle radius $r_M = 0.13 \pm 0.02$ cm is obtained directly from the observed number of discrete scatterers per unit trail length, 100 ± 50 m^{-1}. The shaded areas bounded by these three constraints is the set of particle parameters which agree with the data.

Table 2. Summary of numerical results from analysis of the images of the water-particle trail

Quantity	Magnitude	Comment
Large-particle radius	$r_M = 0.13$ cm $\pm 20\%$ (mean)	"Average" figure; about twice the radius of the nozzle orifice
Large-particle abundance	$f_M = 95\%$ initially, 75% in AMOS views	Adopted, from thermodynamic arguments [6]
Small-particle radius	$r = 0.3\,\mu$m $\pm 0.05\,\mu$m initially	Derived from best-fit to data; then decreases with distance X (Fig. A2)
Small-particle abundance	$f_m = 0.022 \pm 0.007$ of the initially-vented water	Figure 13; derived from constraint from image-plane irradiances in cameras at long and short ranges
Longitudinal particle velocity	$v = 23$ m/s $+6, -8$ m/s	Experimentally indistinguishable from the velocity of the liquid stream
Transverse particle velocity	3–4 m/s nominal average	Little kinetic energy is imparted by the fragmentation of the stream
Small-particle cloud brightness 0.4–0.6 μm $(\eta_1 = 48, \eta_2 = 33)$	$B_m = 2 \times 10^{-6}$ w/cm^2 sr at $X = 1$ km	Figure 12; from I_m and r_0
Large-particle cloud brightness (same view)	$B_M < B_m$ at $X < 2$ km	Figure 12

opaque atmosphere and earth surface (Fig. B1), and (as Appendix B states) these particles are strong absorbers and thus poor reflectors of earthshine, the trail—like some meteorological clouds—would exhibit "negative [infrared] contrast" in nadir-directed views. The thermal emission from individual large particles in the few seconds before they solidify is complicated by their interior temperature gradients; on the other hand their opacity after they become completely frozen wipes out the infrared spectral structure [19] that smaller isothermal ice droplets would exhibit.

The daytime solar near-ultraviolet radiances in projections to distant cameras would be dominated by the small-particle component, with the surface radiances of the trail decreasing less rapidly with X as these particles transition into the Rayleigh-scatter range later along their flight path.

8. PHYSICAL CONTAMINATION OF ORBITER

The images from onboard show no evidence of any of the large particles flowing backward in the frame of reference of the orbiting spacecraft to recontact its body; all move outward, with sensibly the same speed. The lifetimes of these ice drops are several hr (Appendix B), which is sufficiently long for the very largest of them to have finite probability of colliding with space shuttle on subsequent passes when they are in certain posigrade trajectories [2]. Since the short-lived submicron particles have essentially the same downstream velocity, they also would not return to contaminate the spacecraft.

These intensified video photographs do not resolve the unrecondensed gaseous water (its Rayleigh scattering is very weak compared with that of the $2\pi r/\lambda \approx 2$ condensation particles), nor do the optical data provide direct information about the rates at which this vapor is evolved. As the gas is initially collisional [7,9] with mean thermal speeds much

greater than the directed retrograde velocity of the cloud of particles, a substantial fraction of it recontacts vehicle outer surfaces. (At low orbital altitudes the return flux would be increased by backscattering from the atmosphere [5].)

9. CONCLUSIONS

Table 2 summarizes the numerical results of this analysis of the low light level video photographs of vented supply water. The photometric-photogrammetric data lead to the following principal interpretations of the phenomenology of release of narrow streams of liquids (in this case water) in space:

1. *Product states*. The initially-bundled column forms within ~1 m into a bimodal particle size distribution: irregular water/ice drops produced in a cavitational breakup with a mean diameter exceeding that of the venting orifice (~2 mm), and 0.3-μm radius ice spherules produced by partial recondensation of overexpanded water vapor. This vapor represents 20–25% of the mass of water released into near-vacuum.

2. *Spatial distribution*. The angular spreads of the two particle sizes are the same, indicating that the two types of particles have the same velocity components. The longitudinal velocities of the most readily identifiable large particles are experimentally indistinguishable from that calculated for the water stream beyond its conical venting nozzle. The small divergence of the wake trail ($\pm 1/5$ radian) shows that the translational energy imparted to the water mass when bubbles of steam and dissolved gases erupt through its surface is substantially less than the kinetic energy with which it had been discharged.

3. *Particle geometry, temperature, emissivity*. The submicron particles initially formed following the venting sublimate by absorption of sun- and earthshine (the vapor is not optically detectable). Their

mass-loss rates are consistent with standard Rayleigh–Mie theory for ice spheres when a correction for the progressive roughening of their surfaces is applied to their emissivities. These sunlit small particles reach a quasi-equilibrium temperature near 180 K in ~1 2 s, well before they transition into the Rayleigh-scatter regime. The larger particles lose only a negligible fraction of their mass while they remain with the fields of view of the video cameras.

4. Absolute concentration. We estimate the mass fraction of the recondensate to be ~0.1 of the sublimed-vaporized water. This small amount of material dominates the solar-scatter radiances measured by the groundbased telescope-camera over the full detectable length of trail.

5. Physical and optical contamination. We observed no evidence for the movement of the ice particles backwards in such a way as to strike Orbiter surfaces directly. The calculated (in Appendix B) lifetimes of the initially-large droplets are long enough for some to be encountered on later orbits. In contrast, it is predicted that some vapor moves in the posigrade direction, eventually engulfing the spacecraft. This local environment has implications for the design of future spaceborne experiment platforms, in particular Space Station, as well as for infrared astronomy and surveillance from earth orbiting vehicles that dump liquids.

Planned future measurements on water venting from space shuttle include onboard photography with precisely-known pointing and higher spatial resolution, to reduce the uncertainty in the initial longitudinal velocity of the distinguishable particles; inclusion of additives to increase the scattered-light signal; and photometry at a series of solar-scatter angles (from both the ground station and Orbiter's Remote Manipulator Arm) and Mie polarization-ratio measurements (as in [10]) to better determine the dimensions and abundance of the unresolved ice particles.

REFERENCES

1. C. P. Pike, D. J. Knecht, R. A. Viereck, E. Murad, I. L. Kofsky, M. A. Maris, N. H. Tran, G. Ashley, L. Twist, M. E. Gersh, J. B. Elgin, A. Berk, A. T. Stair Jr, J. P. Bagian and J. F. Büchli. Release of liquid water from the space shuttle. *Geophys. Res. Lett.* **17**, 139–142 (1990).

2. M. E. Fowler, L. J. Leger, M. E. Donahoo and P. D. Maley. Contamination of spacecraft by recontact of dumped liquids. *Proc. Third Annual Symp. on Space Operations, Automation, and Robotics (SOAR 89),* NASA Conf. Pub. CL-3059, 99–104 (1989).

3. J. S. Pickett, N. D'Angelo and W. S. Kurth. Plasma density fluctuations observed during space shuttle orbiter water releases. *J. Geophys. Res.* **94**, 12081–12086 (1989).

4. D. G. Koch, G. G. Fazio, W. Hoffman, G. Melnick, G. Reike, S. Simpson, F. Witteborn and E. Young. Infrared observations of contaminants from shuttle flight 51-F. *Adv. Space Res.* **7**, 211–219 (1987).

5. E. Murad. Implications of mass spectrometric measurements on space shuttle. *Planet. Space Sci.* **33**, 421–423 (1985).

6. P. A. Bernhardt. A critical comparison of ionospheric depletion chemicals. *J. Geophys. Res.* **92**, 4617–4628 (1987).

7. E. P. Muntz and M. Orme. Characteristics, control, and uses of liquid streams in space. *AIAA J.* **25**, 746–756 (1987).

8. T. T. Kassal. Scattering properties of ice particles formed by release of H₂O in vacuum. *J. Spacecraft Rockets* **11**, 54–56 (1974).

9. H. Fuchs and H. Legge. Flow of a water jet into vacuum. *Acta Astronautica* **6**, 1213–1226 (1979).

10. B. P. Curry, R. J. Bryson, B. L. Seibner and J. H. Jones. Selected results from an experiment on venting an H₂O jet into a high vacuum. Arnold Engineering Development Center, Tullahoma, Tenn., Tech. Rep. AEDC-TR-84-28 (1985).

11. B. P. Curry, R. J. Bryson, B. L. Seibner and E. L. Kiech. Additional results from an experiment venting an H₂O jet into a high vacuum. Arnold Engineering Development Center, Tullahoma, Tenn., Tech. Rep. AEDC-TR-85-3 (1985).

12. L. A. Freedman. The space shuttle closed circuit television system. *Proc. IEEE National Aerospace and Electronics Conf.,* pp. 23–30 (1981).

13. Avco Research Laboratory (Everett, Mass.). AMOS Users Manual. Private communication.

14. F. X. Kneizys, E. P. Shettle, W. O. Gallery, J. H. Chetwynd, L. W. Abreu, J. E. A. Selby, S. A. Clough and R. W. Fenn. Atmospheric transmittance/radiance: computer code LOWTRAN 6. Air Force Geophys. Lab Tech. Rep. AFGL-TR-83-0187 (1983).

15. H. Patashnick and G. Rupprecht. Sublimation of ice particles in space. Martin-Marietta, Denver, Colo. Tech. Rep. ED-2002-1654, pp. 45–49 (1973).

16. R. D. Sharma and C. Buffalano. Temperature and size histories of liquid H₂O₂ and H₂O particles released in space. *J. Geophys. Res.* **76**, 232–237 (1971).

17. S. G. Warren. Optical constants of ice from the ultraviolet to the microwave. *Appl. Opt.* **23**, 1206–1223 (1984).

18. C. F. Bohren and D. R. Huffman. *Absorption and Scattering of Light by Small Particles.* Chap. 4. Wiley, New York (1983).

19. W. T. Rawlins and B. D. Green. Spectral signatures of micron-sized particles in the shuttle optical environment. *Appl. Opt.* **26**, 3052–3060 (1987).

APPENDIX A

Sublimation and Temperature History of the Submicron-Diameter Particles

Heat balance

The daytime energy budget of liquid or solid water in the low earth orbital environment is made up of the three terms absorption of earthshine and direct sunlight, thermal re-radiation, and the heat loss due to evaporation or sublimation. Heating by sunlight scattered from the atmosphere is small because the atmospheric water vapor absorbs over much the same spectral regions as solid or liquid water; multiple scattering within the wake trail can be neglected

because the trail is optically thin; and collisional heating of particles with radius $> \sim 0.01\,\mu$m is negligible at orbital altitudes. The temperature can be considered uniform throughout submicron ice droplets, as their high thermal diffusivity ($\sim 10^{-2}\,$cm^2 s) leads to isothermality in microseconds.

The rate of change of temperature dT/dt of smooth-surfaced, spherical submicron ice particles with uniform radius r can therefore be written [15,16]

$$\frac{4\pi}{3} r^3 \rho C \frac{dT}{dt} = \int \epsilon(r,v)\Omega_e r^2 q_e(v)\,dv$$

$$+ \int \epsilon(r,v)\Omega_s r^2 q_s(v)\,dv$$

$$- \int \epsilon(r,v)\Omega_p r^2 P(v,T)\,dv$$

$$+ 4\pi r^2 \rho L \frac{dr}{dt}. \qquad (A1)$$

The symbols and their numerical values where appropriate are

ρ = density = 0.92 g cm^3

C = average specific heat (at constant volume) of ice between 250 K and 180 K = 1.9 J gK(= 0.45 cal gK)

L = average heat of sublimation of ice over this temperature range = 2.4×10^3 J g

v = frequency of emitted/absorbed electromagnetic radiation

$\epsilon(r,v)$ = particle emissivity ("effective" emissivities are defined immediately below)

$P(v,T)$ = Planck radiation function = $2hc^{-2}v^3(e^{hv/kT} - 1)^{-1}$, where c, k, and h have their conventional meanings

$q_e = P(v,T_e = 280\,$K), for the earth approximated as a 280 K blackbody

$q_s = P(v,T_s = 5800\,$K), for the sun approximated as a 5800 K blackbody

Ω_e = solid angle subtended by the earth at the 329-km altitude particle $\approx 1.4\,\pi$ sr (taking into account the infrared opacity of the atmosphere above the hard Earth surface)

Ω_s = solid angle subtended by the sun at the particle = 6.8×10^{-5} sr

Ω_p = solid angle into which the particle radiates (isotropically) = 4π sr.

The small variations with temperature of C and L and the approximation of the sun and earth as blackbody radiators have only an insignificant effect on the numerical results. In addition the initial temperature T_0 of the recondensation droplets is uncritical, as it does not affect the final equilibrium temperature and—in view of the initial very high cooling rates by evaporation and sublimation—has only a very small effect on the time to approach this equilibrium; we adopt the 250 K of the water vapor from the phase diagram reproduced in the report of a laboratory simulation [9], and consider only the solid phase.

We derived "effective" emissivities for earthshine (ϵ_e), the thermal radiation from the particle (ϵ_p), and sunlight (ϵ_s) by first weighting and averaging the imaginary component of the index of refraction of ice [17] at 266 K over each blackbody distribution at the appropriate radiating temperature. (For ϵ_p, we used the range of temperatures predicted by initial approximate calculations.) The variation of the complex index of refraction with temperature (and ice crystal structure), and the experimental uncertainty of this quantity over part of the infrared [17], introduce a small error into the emissivities. We then applied standard Mie theory [18] for spherical particles with size parameter $2\pi r/\lambda < 1\,n$, where λ is wavelength and n the real part of the index of refraction. This condition holds for $r < \sim 1.3\,\mu$m since most of the earthshine absorption (the major factor in

heating) and re-radiation takes place at wavelengths above 10 μm, and also for sunlight absorption, which is principally at wavelengths near 3 μm. Typical effective emissivities, for $r = 0.20\,\mu$m, are 2.6×10^{-2}, 2.0×10^{-2} (at 180 K particle temperature, and about 10% higher at 200 K), and 0.26 $\times$ 10^{-2} respectively.

Equation (A1) can thus be simplified to

$$\frac{4\pi\rho}{\sigma}(rC\dot{T}/3 - L\dot{r}) = \epsilon_e\Omega_e T_e^4 + \epsilon_s\Omega_s T_s^4 - \epsilon_p\Omega_p T^4. \quad (A2)$$

where the dots denote time derivatives and $\sigma = 5.7 \times 10^{-12}$ J s cm^2 K^4 is the Stefan–Boltzmann constant.

Temperature

The exponential dependence on temperature of the equilibrium vapor pressure P of liquid and solid water ($P_{torr} = 2.4 \times 10^{10} \exp - [6110/T]$) provides insight into the cooling process, since the sublimation rates per unit exposed area are proportional to this pressure (except at the initial very high temperatures, where the water gas is collisional and thus partially recondenses on the particles). This sublimation is initially the principal energy loss mechanism. Similarly, the very rapid evolution of water vapor from the surface of the bundled stream and its fragmentation droplets results in most of the recondensation particles being formed within a few 10's of meters— $< \sim 5$ seconds flight path— from the spacecraft (see Appendix B). As the particle temperature drops $L\dot{r}$ also decreases, and since the right-hand side of eqn (A2) is changing slowly $\dot{T}$ decreases also. Substitution of L and C into the left-hand terms of eqn (A2) shows that the fractional decrease in particle radius is $\sim 1/3000$ per K during the period when sublimation is the dominant energy loss mechanism; therefore a decrease in temperature from 250 to near 200 K expends less than 2% of the initial radius of the small droplets.

The spectral emissivity of weakly-absorbing spheres is proportional [18] to r when $\sim 0.01 < 2\pi r/\lambda < 1\,n$; that is, $\epsilon \sim k/r$, where i represents e, p, or s in the above notation. Substitution into eqn (A2) then results in the further simplification

$$r\dot{T} - \xi\dot{r} = \gamma r - \delta rT^4, \qquad (A3)$$

where $\xi \equiv 3L/C$, $\gamma \equiv (3\sigma/4\pi\rho C)\cdot(k_e\Omega_e T_e^4 + k_s\Omega_s T_s^4)$, and $\delta \equiv 3\sigma k_p/\rho C$ are constants. The Mie calculations showed that $k_e = 1.3 \times 10^3$ cm^{-1}, $k_p = 1.0 \times 10^3$ cm^{-1} (at 180 K), and $k_s = 0.13 \times 10^3$ cm^{-1}.

A second relationship between radius and temperature of the particles can be derived from the above-mentioned dependence of their sublimation rate on vapor pressure and temperature. When the ambient pressure near the surfaces of individual particles is so low that the probability that departing molecules return is small [that is, the collisional mean free path in this nearby gas (and particle cloud) exceeds the particle diameter], the rate of change of radius by sublimation becomes [7,15]

$$\dot{r} = 0.27P(T)/T^{1/2}. \qquad (A4)$$

We solved coupled nonlinear differential eqns (A3) and (A4) using the fourth-order Runge–Kutta numerical iteration method, keeping the k's independent of time and particle radius. With the initial radius $r_0 = 0.3\,\mu$m and temperature $T_0 = 250$ K taken as the constants of integration, the particles cool to 180 K within 1 s, after which their temperature shows an almost constant rate of decrease at ~ 1.20 K s^{-1} to 120 s; refer to Fig. A1.

Radius loss rate

These results, as noted, would apply to monodisperse ice spheres whose emissivities are proportional to r; only the initial cooling times depend (weakly) on the r_0 and T_0
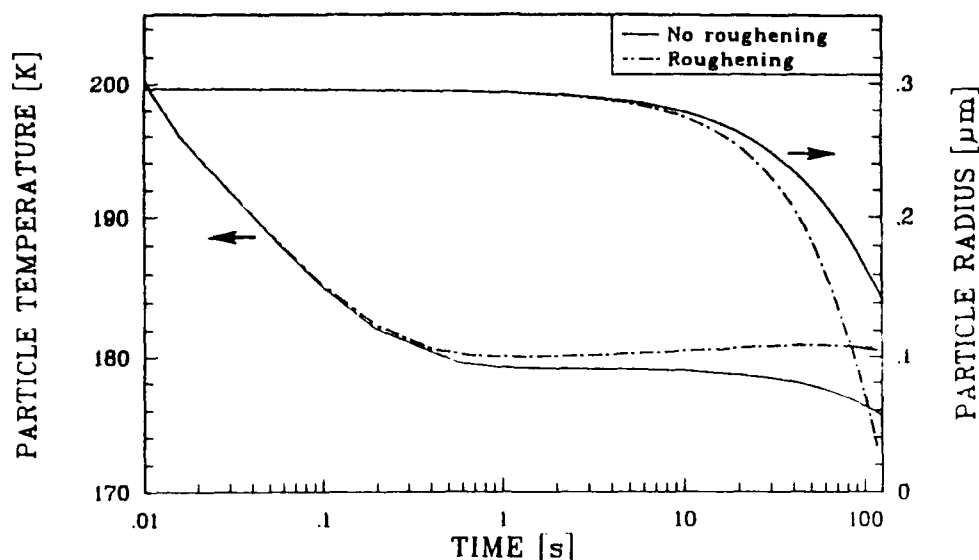
Fig. A1. Temperature and radius of the recondensation ice particles calculated without and with the progressive surface roughening parameters in Fig. A2 (refer to the text).

adopted. We consider next the decrease of radius of these particles with distance from the venting orifice, which requires two further inputs: the dependence of this distance on time after the particles form and, for comparison with the radiance data in Fig. 6, the effective cross-section of these particles for scattering of solar photons in the direction of the AMOS camera.

For the reasons stated in the text, we adopt the (constant) longitudinal velocity of the distinguishable large water-ice droplets measured from the onboard photographs as the velocity of the small particles. Thus their time-since-formation at downstream distance X in the groundbased images is inversely proportional to this velocity. (The 10's-m distance from the venting orifice over which the water gas evolved from the liquid recondenses is so small relative to the distances resolvable from AMOS that it can be neglected.)

We calculated the differential scattering intensities of ice spheres of radius r at $\eta_1 = 48$ (averaged over $\pm 2^\circ$, to minimize any effect of Mie resonances) weighted for the product [solar spectral irradiance] [S-20R wavelength response of the telescope-camera] [transmission of the clear-night atmosphere above AMOS at the 61 zenith angle of the particle trail (calculated by LOWTRAN [14]; increasing by about 15% between 0.4 and 0.65 μm)]. This illumination-times-system response factor is shown in Fig. 10, and the differential scattering cross-sections per unit projected (sub-micron) particle area derived from it are in Fig. 11. This wavelength-weighted photometric function can be seen to be relatively insensitive to particle radius down to 0.25 μm (the "geometric" range), after which it decreases about linearly to $r = 0.15 \mu$m, where it begins to exhibit the expected Rayleigh-like ($r^{3.8}$) behavior. We fit the first two segments of this function with a cubic spline in calculating
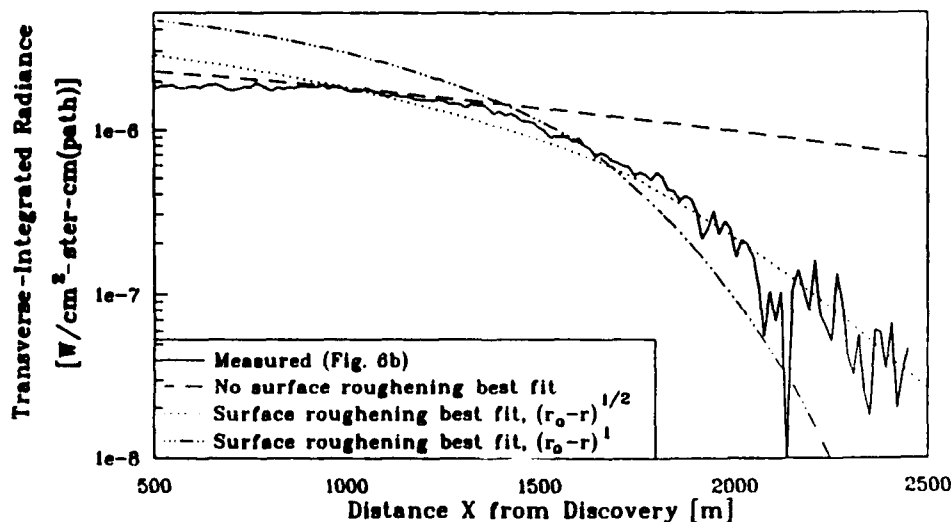

Fig. A2. Measured [Fig. 6(b)] and calculated transverse-summed radiances of the wake trail in the AMOS images at $\eta_1 = 48$. Particle emissivities $\varepsilon_1 = k_1 r (1 + 2.1 \mu m^{-1.2} [r_0 - r]^{1.2}/r)$ with $r_0 = 0.30 \mu$m resulted in the best fit with surface roughening. A linear dependence of the change in emissivity on Δr can be seen to produce a substantially poorer fit.

the dependence on X of the on-axis and transverse-summed sunlight-scatter radiances.

Since both the total number per unit pathlength and initial radius r_0 of the vapor-recondensation particles are yet to be determined, a normalization of the calculated summed radiances at one downstream distance and in absolute value is necessary. (r_0 is as noted a constant of integration of the rate equations, and the absolute brightnesses are normalized by a multiplicative factor.) The manual best-fit to the radiances in Fig. A2, in which $r_0 = 0.3\,\mu$m, shows that beyond about halfway along the detectable trail image the radius (which is plotted in Fig. A1) is decreasing substantially faster than is predicted by our energy balance-Mie scattering calculation. The difference between the observed and calculated solar-scatter radiances would be larger if the velocity of the small recondensation particles were greater than that of the stream-fragmentation droplets; in any case, however, a systematic error from this velocity—a multiplicative effect—would not substantially improve the fit to the data. This discrepancy between (actually straightforward) theory and the AMOS measurements indicates that the particle temperatures and radii shown as solid curves in Fig. A1 can not be correct.

Surface roughening

A larger sublimation rate would result from progressive roughening of the surfaces of ice droplets exposed to vacuum, a phenomenon that has been observed in the laboratory [15]. This roughening is interpreted [15] as increasing the emissivities of the ice particles through multi-phonon interactions [it may be viewed as enhancing the number of vibrational modes of the now-irregular droplets that are accessible to the incident electromagnetic wave(s)], rather than by increasing the outer-surface area of somewhat "spongy" particles. Vacuum-tank experiments with ~ 10's-micron such droplets [15] showed that this relative rate of loss of radius itself increases as the particle ages, which is also in qualitative agreement with the dependence of radiances on X shown in Figs 6 and A2.

We therefore repeated the calculation with the three particle emissivities absorptivities $\bar\epsilon$ increased by a term $k\,\beta(r_0 - r)^{1\,\text{or}\,1\,2}$, where β as well as r_0 is empirically determined by fitting to the measured transverse-summed trail radiances. [The computational model with this perturbation still implicitly assumes that the ice particles are spherical, through the Mie scattering of wavelength-weighted sunlight, the sublimation rate at fixed temperature eqn (A4), and terms in eqn (A3).] The idea that the increase in each of the emissivities would depend on the square root of the decrease in the initial radius of the particle follows from the perceived "statistical" nature of the irregularities produced when the particle surface erodes; this functional form in fact results in a rather better manual fit to the AMOS data than a linear dependence on $[r_0 - r(t)]$, as Fig. A2 shows. This best-fit was derived with $r_0 = 0.30\,\mu$m, $\beta = 2.1\,\mu$m$^{1\,2}$.

While this analytic form of the increase in the effective emissivities is not necessarily unique, an acceleration of the fractional rates of mass loss during the transit of the particles through the AMOS camera's field is definitely indicated by the curvature as well as the slopes in the plot of log (sterance) against X. The fit that results from the hypothesis that the increase in emissivities depends on the change in particle radius is not substantially different from that in our preliminary analysis [1], in which we applied the less physically-realistic assumptions that the rate of change of fractional particle radius increases linearly with time (or X) and that the total cross-section for scattering of sunlight undergoes a distcontinuous change from purely geometric (r^2) to Rayleigh (r^6) at the downstream distance at which the slope of the integrated radiances in Fig. A2 appears to change.

The resulting radii and temperatures of initially-monodisperse $0.3\,\mu$m recondensation ice particles are shown as dash-dot curves in Fig. A2. A minimum at slightly above 180 K is reached within 1 s, after which the particle temperature actually increases by about 1 C over the remaining ~ 100 s ($2\frac{1}{2}$ km) of detectable trail; this increase is due principally to the particles absorbing more earthshine radiation per unit mass as their surfaces progressively roughen. The mean particle radius by this time has decreased to $0.05\,\mu$m. The alteration of temperature by roughening about doubles the rate of decrease of radius beyond ~ 50 s— 1000 m from *Discovery*—, as can be readily seen from the dependence of P on T [and eqn (A4)].

APPENDIX B

Temperature History of the Millimeter-Diameter Particles

Emissivity and heat conduction

Energy balance eqn (A1) also applies for estimating the temperatures and decrease in volume by evaporation, sublimation of the large water droplets. In the interest of simplicity, we consider only a single ("mean") initial radius of assumed-spherical, non-fragmenting or cracking particles, which we take to be the 0.13 cm derived in the text.

These stream rupturing-product particles differ in emissivity from the vapor-recodensation ice particles, as to a good approximation they are black bodies over the infrared wavelengths at which they absorb earthshine and radiate thermally; that is, $\epsilon_e = \epsilon_p \approx 1$, independent of radius r. In consequence reflection of IR earthshine by these large particles is small compared with their thermal emission, and since their equilibrium temperature is less than the ~ 280 K of the optically-thick atmosphere and earth (as will be shown shortly) the artificial cloud would exhibit "negative [infrared] contrast" when viewed in the nadir.

We averaged the emissivity-absorptivity $\bar\epsilon$, over the spectrum of sunlight, finding $\bar\epsilon$, to be 0.15 at $r = 0.13$ cm (and about proportional to r). As this particle radius undergoes only a small fractional change during the first few km of flight path relative to the spacecraft all three emissivities can be taken as constant, substantially simplifying the calculations. (The issue of surface roughening is moot in view of these large emissivities.)

This advantage is in large part offset by a second major difference in the energy balances of the two size particles: in the large droplets, the time scales for temperature equilibrium by conduction are long compared with the characteristic times for sublimative-evaporation loss of heat from the droplet surfaces. The time step in the early cooling stages (when the temperatures and therefore vaporization rates are high, as was shown in Appendix A) is therefore controlled by transport of heat from the interior. (The resulting radial temperature gradient introduces some uncertainty into the thermal emission rates during this period, since the outermost "shell" is not optically thick at all the principal wavelengths radiated; and the difference between the indexes of refraction of liquid and solid water adds a small further uncertainty to the scattering and absorption cross-sections in the period before the particles freeze completely.)

Cooling considerations

The initial temperature of the droplets can be estimated from the rates of evaporative cooling of the surface of the cylindrical stream before it fragments [7] and the effective thickness of this cooled outer annulus. Since the near-surface temperature of the coherent stream is decreasing only logarithmically with time [7] (the volume is also not isothermal), the exact distance from the venting orifice at

which rupturing takes place is uncritical. With this distance estimated from the onboard video images (and laboratory simulations [9]) as 1 2 m the lifetime of the bundled stream is 2×10^{-3} s. During this period its surface temperature falls from the initial 303 K — the nominal ejection temperature, which is similarly uncritical—to about 250 K [7]. (Convective mixing accompanying the violent cavitational fragmentation could be expected to momentarily melt any ice that may have formed near the surface of the stream.)

The radial thickness of this annular heat "diffusion layer" is to a good approximation

$$[(4 \pi)(\text{diffusivity } K \text{ of } \sim 275 \text{ K water}) \cdot 2 \times 10^{-3} \text{ s}]^{1/2}.$$

This diffusivity K [$\equiv$ (thermal conductivity) (density) (specific heat)] is 0.0014 cm^2 s. Thus the thickness of this outer shell is 0.06 mm, which is closely 1/10 of the radius of the relaxed stream calculated in Section 4.2.2. A mean initial temperature of these water droplets would therefore be 303 K — (2 × 0.1 × [(303 − 250) 2])K ≈ 298 K. The fraction of the vented water mass evaporated in this pre-breakup period which produces this 5 C mean temperature change is 0.01. As the total fraction that vaporizes to cool and freeze the remaining water is only about 0.2 the small change in mean radius—7%—again neglecting the difference in density between ice and liquid water—justifies its neglect in estimating the fraction of vented water recondensed into small particles (in Section 6). The higher thermal conductivity and lower specific heat of pure ice give it a heat diffusivity almost nine times that of pure liquid water near 0 C; therefore the characteristic heat transport times decrease by an order of magnitude after the particles solidify (assuming that advective transport in the liquid can be neglected [7])

We calculated the surface temperature of these infrared-opaque large particles by iteratively solving the energy-balance and sublimation-rate eqns (A1 2) and (A4), taking into account the interior temperature gradients. The principal source of heat input is earthshine, that is, $\Omega_+ T_+^4 > 0.15 \Omega_+ T_+^4$. Within the first few seconds after the coherent stream fragments, while the surface temperature and vapor pressure remain high, the loss of heat is effectively all due to evaporation sublimation. We equated this evaporative

loss during cooling time interval Δt with that resulting from the decrease in temperature of an outer spherical shell of thickness Δr, which we approximated as $(K \Delta t)^{1/2}$. The flow of heat through this layer (whose thickness eventually becomes comparable with r) determines the initial time scale of cooling of the large water ice particles.

When this outer shell is liquid, this equation can be stated as

$$(4\pi\ 3)(r^3 - [r - \Delta r]^3)\rho_w C_w \Delta T$$
$$= (4\pi\ 3)(r^3 - [r - \dot{r}\ \Delta t]^3)\rho_w L_w \quad \text{(B1)}$$

where ρ_w, C_w, and L_w are the parameters defined in Appendix A for liquid water (L_w is a heat of vaporization from the liquid). Since $\Delta r\ r$ is initially much less than 1 (as we found above), this expression reduces to the even more intuitively obvious

$$\Delta r C_w \Delta T = \dot{r} \Delta t L_w \quad \text{(B2)}$$

When the droplet surface begins to solidify, two further terms added to the left-hand side of eqn (B2) take into account the phase transition from liquid to solid in an immediately-inner spherical shell and the cooling of the outer layer of ice

$$\Delta r_w C_w \Delta T + H(K'\Delta t)^{1/2} + \Delta r_i C \Delta T = \dot{r} \Delta t L. \quad \text{(B3)}$$

Here Δr_w and Δr_i represent the thicknesses of these concentric liquid and solid shells. H is the heat of fusion of water (which we took as constant at 80 cal g), and ρ_w is again approximated as ρ.

We solved eqns (B2) and then (B3) iteratively down to 200 K with temperature step $\Delta T = 1$ C. Near this temperature the thickness of the effectively-cooled layer reaches ~ 1.4 of the particle radius, and the radiative cooling terms are becoming comparable with the (essentially exponentially decreasing) sublimative cooling term. We therefore assumed isothermality (homogeneous cooling) below 200 K, and determined the time dependence of temperature by the iterative procedure applied in Appendix A to the small ice particles
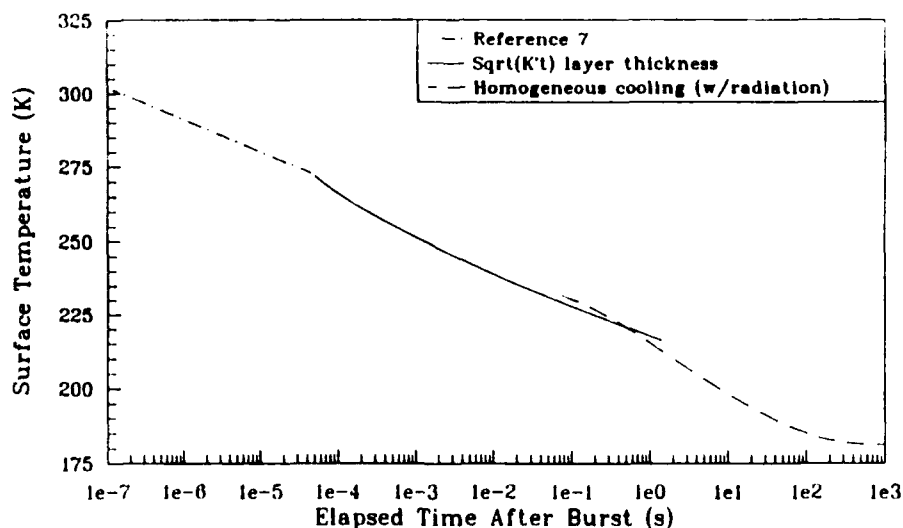

Fig. B1 Surface temperature history of the ~mm ice particles. Outer shell cooling is calculated for the first second after burst (solid line), after which bulk particle cooling (isothermality) is reached (dashed line). The initial extremely rapid cooling (times < ~10⁻³ s) follows from an iterative solution of a one dimensional diffusion equation with the stream modeled as a semi-infinite slab [7].

Results

The calculated dependence on time of the outermost-surface temperature of the large droplets is shown in Fig. B1. (The extremely ra~·d decrease to ~250 K is taken from a calculation with a different geometry [7]; in any case, the time in which this surface temperature is reached is ≪ 1 s.) This temperature falls to 200 K in about 10 s, when these particles have moved some 200 m from the venting nozzle. They then asymptotically approach 181 K in (coincidentally) the remaining ~100 s of their path during which the accompanying cloud of small ice particles remains above the detection threshold of the AMOS telescope-camera.

With this equilibrium temperature eqn (A2) gives $dr/dt = 4 \times 10^{-6}$ cm/s. The characteristic fractional decay time $(dr/r\,dt)^{-1}$ of the stream-fragmentation particles is therefore 3×10^4 s, or 5 low earth orbital periods (during which the orbits decay significantly [2]). This is considerably longer than the effective lifetime of the four orders of magnitude smaller vapor-recondensation particles indicated in Fig. A2.